December 2019

Numerical Simulation of Droplet Formation in a Microfluidic Ice Nucleating Particle Measurement Device

Ali Mohammadi Nafchi
Clemson University, ali.mnafchi@gmail.com

Recommended Citation

Mohammadi Nafchi, Ali, "Numerical Simulation of Droplet Formation in a Microfluidic Ice Nucleating Particle Measurement Device" (2019). *All Theses*. 3228.
https://tigerprints.clemson.edu/all_theses/3228

NUMERICAL SIMULATION OF DROPLET FORMATION IN A MICROFLUIDIC ICE NUCLEATING PARTICLE MEASUREMENT DEVICE

A Thesis
Presented to
the Graduate School of
Clemson University

In Partial Fulfillment
of the Requirements for the Degree of
Master of Science in
Biosystems Engineering

---

by
Ali Mohammadi Nafchi
December 2019

Accepted by:
Dr. Andrew Metcalf, Committee Chair
Dr. Terry Walker, Committee Co-chair
Dr. Christophe Darnault
Dr. Ehsan Mousavi

ABSTRACT

Ice nucleating particles have a great impact on weather and climate by affecting the freezing process of water in the atmosphere. Therefore, INP measurements are essential to developing more accurate climate models. Despite of the importance of INP measurements, available measurement techniques are costly, which leads to scarcity of available data. Microfluidic technology offers unique features including small scales and low fabrication costs; thus, can be used to design and develop an INP instrument with lower operation costs, which can enhance the number of INP measurements. In this study, we used a microfluidic platform that can be further developed to an INP instrument. Our initial experiments showed that droplet formation in the microfluidic system can be affected by external factors, such as vibration and heat transfer. We have performed numerical simulations to derive the equations that describe droplet properties (size, generation frequency, and velocity) as a function of flow rate ratio. The derived correlation can be used in designing a future INP measurement device that features a method to keep the consistency of droplet formation. Moreover, the effect of cooling on pressure inside the channel was studied and it was found that cooling increases the pressure inside the channel due to increasing the viscosity of the fluids.

ACKNOWLEDGMENTS

First of all, I would like to thank my advisor, Dr. Andrew Metcalf, who gave me the opportunity to be part of this amazing research. Secondly, I would also like to thank my committee co-chair Dr. Terry Walker for his kind support throughout my graduate studies at Clemson University. Next, I would like to thank Dr. Christophe Darnault, and Dr. Ehsan Mousavi who kindly accepted to serve as my committee members.

Special tanks go to my parents and my brother who encouraged me to begin this journey. Even though they could not be here physically, I have always had their love and support.

Additional thanks go to Bill Delaney, Clemson microfabrication facility manager; Negin Kananizadeh, department postdoctoral fellow, David Lipscomb, department lab manager; Samuel Forrest, safety manager at Department of Research Safety; and Rodney Merck and Rodney Morgan, department lab specialists.

Many others have also played a part in this thesis; those include Walt Williams, Dr. Metcalf's other graduate student; Hamed Torkzadeh, Mojtaba Qanbarzadeh, and Connor Parker, Ph.D. students at the department.

TABLE OF CONTENTS

Page

Table of Contents (Continued) Page

LIST OF FIGURES

Figure Page

List of Figures (Continued)

Figure Page

LIST OF TABLES

CHAPTER 1

Homogenous and Heterogenous Freezing of Water

Water freezes at temperatures below 0° C when a microscopic amount of stable solid phase is present within the bulk of the liquid.[1] This transition from liquid to solid phase requires energy to form an interface between the two phases; thus, it is thermodynamically unfavorable.[2] Suspended or dissolved impurities can act as a catalyst to reduce the energy required for ice nucleation, while mechanical vibrations provide the necessary initiation energy. When impurities are present, the phenomenon is called heterogenous ice nucleation. In the absence of external perturbations, water can be further supercooled to near -41.15 °C before it freezes.[3] Near this temperature, thermally-driven density fluctuations can overcome the energy barrier and form embryos – "a thermodynamically unstable aggregate of water molecules in a structure that favors further development into stable ice"[4] - within the bulk of the metastable liquid.[1] These embryos either decay or grow depending on their size; the possibility of growth of an embryo increases with the embryo size. At a critical embryo size, the possibility of growth and decay becomes equal; therefore, an ice nucleus is probable to be formed beyond this point.[4] This phase transformation is called homogenous ice nucleation. Ice formation in liquid water is one of the most important liquid-to-solid transitions and it has been studied because of its key impacts on many areas of research, including atmospheric chemistry, cloud physics, and precipitation;[5] icing on surfaces such as aircraft wings;[6] food, biosystems, and pharmaceutical industry;[7–9] and cryobiology and life at temperatures below 0°C.[10,11]

Ice Nucleating Particles (INPs), Weather, and Climate

The formation of ice crystals in the atmosphere plays an essential role in the hydrological cycle, earth's energy balance, and climate by affecting physicochemical properties of the clouds.[12–14] Therefore, understanding the parameters that affect ice initiation and evolution in clouds is essential for developing more accurate weather and climate prediction models. Atmospheric particles play a critical role in ice initiation by serving as ice nucleating particles (INPs) and catalyzing the freezing process; leading to heterogenous ice nucleation.[4] Although ice is formed in the atmosphere through both heterogenous and homogenous processes, heterogenous nucleation is considered to be the dominant freezing mode in the clouds.[12] Complex interactions between INPs and supercooled water droplets in mixed-phase clouds lead to various ice nucleation pathways. These pathways include deposition nucleation, immersion freezing, condensation freezing, and contact freezing.[13] Deposition ice nucleation occurs in the absence of liquid water when supersaturated water vapor freezes on an INP surface. Immersion freezing refers to a pathway in which an immersed INP in the liquid droplet initiates ice nucleation.[15] Condensation freezing occurs when water vapor is first condensed on the surface of the INP and freezes afterward. Contact freezing refers to a nucleation pathway in which ice is formed as the result of collision between an INP and a supercooled water droplet.

INP Measurement Techniques

Accurate measurements of INP concentration and understanding the mechanisms by which nucleation is initiated are essential to validate laboratory and modeling studies. However, field measurements of INP are relatively rare and restricted to a few locations with limited temporal coverage.[16,17] Continuous flow diffusion chambers (CFDCs) currently used for in situ INP measurements expose the sample air flow to controlled freezing conditions to generate frozen ice particles.[18] The formed ice particles are then detected optically, and the quantity of detected ice corresponds to INP concentration in the air flow. CFDCs large, heavy, and energy intensive due to the design of the temperature control unit; thus, must be carried by manned research aircraft, which leads to high operational costs to measure spatiotemporal patterns of INP in the atmosphere. As opposed to manned aircraft, Unmanned Aerial Systems (UAS) can provide greater temporal and spatial flexibility while reducing operating costs and, thus, have the potential for use in the future to make ambient INP measurements.[19] However, one challenge remains to be solved: lack of a small, lightweight, and continuous INP measurement platform designed for the UAS-based approach.

Microfluidic Technology

Microfluidics refers to the design and fabrication of systems that feature fluid channels on the order of submillimeter. The application of submillimeter tubes in the industry dates back to the 1950s when nozzle arrays capable of dispensing small amounts of liquids were used in ink-jet printing.[20] Later, in the 1970s, the fabrication of a miniaturized gas chromatograph on a silicon wafer made a breakthrough in molecular analysis techniques, including high-pressure liquid chromatography (HPLC) and gas phase chromatography (GC).[21] This achievement reduced the size and footprint of HPLC and GC instruments. In the 1990s, a series of research projects were supported by the Department of Defense to design and fabricate small microfluidic chips capable of detecting biological and chemical hazards.[22] Microfluidics were later introduced to the field of molecular biology and provided higher sensitivity and resolution techniques for DNA sequencing.[23,24] Further advances in microfabrication technology resulted in the emergence of complex microfluidic chips that include microvalves, micropumps, reaction chambers, and temperature control and sensing units. These systems are termed "lab-on-a-chip". Today lab-on-a-chip systems have numerous applications in single cell analysis,[25] drug delivery,[26] DNA amplification,[27] and diagnostic chips.[28] The wide ranging interest in microfluidics arises from the technology's unique features, including small scales, rapid prototyping, and relatively low fabrication costs.[29]

Droplet microfluidics – a subcategory of microfluidics – enables continuous generation of discrete droplets suspended in a carrier fluid using a variety of configurations, including T-junction, flow-focusing, and co-flowing geometries (Fig. 1). In all of these configurations, droplets are generated as the result of complex interactions between two immiscible fluids.[30] This interaction is affected by the flow rates and physical properties of the phases including density, viscosity, and surface tension.

T-junction. The T-junction configuration (Fig. 1a) was first introduced by Thorsen et al.[31] In this design, the continuous phase flows through the main channel while the dispersed phase is introduced from a perpendicular branch channel.[32] At the junction of the device, the interaction between shear forces and interfacial tension results in the formation of droplets.

Flow-focusing. The flow-focusing microfluidic design (Fig. 1b) consists of three inlet microchannels that merge into a main midchannel and was first implemented by Anna et al.[33] The dispersed phase (reagent fluid) is introduced to the device from the middle channel while the continuous phase (carrier fluid) enters the device from two symmetrical side channels. At the generation region where the two phases meet, symmetric shearing forces – caused by the continuous phase – break the dispersed phase into a consistent series of droplets.

Co-flowing. The co-flowing geometry (Fig. 1c) was first implemented by Cramer et al.[34] and consists of a capillary nozzle inside a microfluidic channel. The dispersed phase is introduced into the continuous phase flow through the nozzle. In this configuration, droplets only form if the continuous phase velocity increases beyond a critical value. Below this value, shear and pressure forces cannot overcome the interfacial tension to form a droplet.[35]

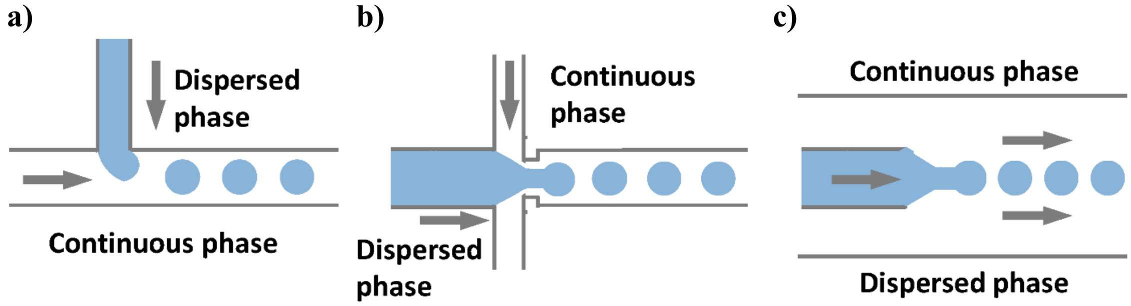

Figure 1. Schematic of different droplet microfluidic configurations including T-junction (a), flow-focusing (b), and co-flowing (c). Figure adopted from Ma et al. (2017).[36]

In a lab-on-a-chip device, these droplets are transferred downstream to a processing region where they are treated as a microreactor in which physical, chemical, or biological reactions can occur.[37] A relatively high surface-to-volume ratio of the droplets guarantees rapid heat and mass transfer, which leads to faster reactions.[38] Continuous measurements in these systems allow rapid repeatability of experiments, which provides a buildup of statistics in a significantly shorter time compared to traditional experimental methods.[2]

Precise Control over Droplet Formation

A large number of experimental and numerical studies has been performed to identify methods which can be used to control droplet formation. These methods include adjusting fluid flow rates or velocities,[39] and manipulating the temperature of the droplet formation region.[40] Changing the flow rates directly effects the interaction between the fluids by changing the magnitude of shear forces while manipulating nozzle temperature changes fluid temperature-dependent physical properties. These properties include viscosity, density, and interfacial tension, and previous studies have shown their effect on droplet formation.[41–43]

Although manipulating the nozzle temperature is an option to control droplet formation, changing the flow rates is still the easiest and most practiced method to obtain the desired droplet size, generation frequency, and velocity. The only drawback of this method is that these droplet parameters cannot be controlled independently by changing the flow rates. This means only a specific combination of droplet size, velocity, and generation frequency can be obtained in a specific droplet microfluidic geometry.

In a variety of microfluidic applications, downstream heat transfer is used as an external controllable factor to manipulate droplets' physical properties.[44–46] Downstream heating has been used to sort droplets and increase the mixing efficiency within them. Lee et al. used a temperature control system integrated into a microfluidic device to measure the temperature-dependent interfacial tension between two immiscible fluids.[47] Ting et al.[48] investigated droplet breakup by embedding a microheater far downstream of a symmetrical micro-bifurcation device. Size of daughter droplets were controlled by adjusting the heater temperature. Baroud et al.[49] showed that heat from a laser beam can act as a thermocapillary valve to block the motion of the oil-water interface in a microfluidic channel. They also showed that this method can be integrated into complex microfluidic systems to sort droplets. Yesiloz et al.[50] placed a resonator as a local heating source in a microfluidic channel to investigate the mixing efficiency inside single droplets. The heat produced by the resonator causes three-dimensional motion inside droplets, which results in fast mixing. Ho et al.[51] used a 3D numerical model to investigate the thermo-coalescence of droplets in a T-junction microfluidic device. They concluded that droplet velocity in the channel is a function of temperature; therefore, at a critical temperature, an individual droplet can be trapped inside a heated chamber. In another study, Khater et al.[52] investigated volume and stability of droplets as they travel over a heating source placed far downstream from the droplet generation region both experimentally and numerically. In all the above applications, external heating was used as a parameter to manipulate the droplet transport in microchannels., Downstream cooling has been mainly used in droplet microfluidic systems to study ice nucleation and kinetics and freezing biological substances. Laval et al.[53] and Teychené et al.[54] used a microfluidic platform to store monodispersed droplets exposed to cooling to study nucleation kinetics. Stan et al. developed a microfluidic system capable of continuously measuring homogenous freezing temperature of water.[2] Although continuous measurements require precise droplet formation control, there is a lack of study on the effects of downstream cooling on droplet formation.

Droplet Microfluidics for INP Measurements

Droplet-based microfluidic systems have the potential for use in UAS for INP measurements. Small, lightweight microfluidic devices are capable of generating microdroplets, freezing them, and measuring the temperature at which they freeze. These systems must have the capability to be coupled with a collector to continuously sample INPs in the ambient air, run the analysis, and provide real-time results. The advantages and disadvantages of a proposed microfluidic device in comparison to currently available INP measurement techniques are listed in Table 1.

Table 1. Summary of advantages and disadvantages of INP measurement techniques.[13,55,56]

Approach	**Advantages**	**Disadvantages**
Portable chambers (e.g. CFDC)	- Mimic real atmospheric processes - Can measure temperatures below water homogenous freezing limit - INPs can be separated and analyzed - Semi-continuous measurements	- Large size and heavy - High power requirement - Limited sensitivity (related to sample volume) - High operational costs - Labor intensive

Approach	Advantages	Disadvantages
Offline analysis	- Flexible and easier sampling - Relatively inexpensive	- Sampling and storage may affect the analysis - Labor intensive - Offline technique, not a continuous measurement
Microfluidic chip	- Small and lightweight - Low power consumption - Inexpensive - Continuous measurements	- Unclear, possible interaction between carrier fluid and the sample

Technical Approach for Microfluidic INP Measurements

Stan et al. (2009)[2] developed a lab-on-a-chip microfluidic platform that integrates droplet microfluidics with cooling processes to measure the homogenous freezing temperature of water (Fig. 2). The platform includes a flow-focusing microfluidic device to generate water droplets in a liquid fluorocarbon carrier and an extended straight microchannel for temperature processing. The device is mounted on a stage that features three separate temperature-stabilized zones. The first zone (inlet hot zone) keeps the droplet formation region at a constant temperature to assure consistent droplet generation. The second zone (cold zone) cools the droplets to freezing temperature, and the third zone (outlet hot zone) melts the frozen droplets to prevent any accumulation of ice to avoid clogging. A coolant fluid (ethanol) is pumped through the copper zones of the stage to cool down the cold zone. Temperature of each zone is precisely set using thermo-electric controllers. A high-speed CCD (charge coupled device) camera is mounted on a stereo microscope to capture images of the droplets' transport and freezing phenomenon. The exact location of the channel where droplets freeze is determined by analyzing the captured images; and an array of platinum residence temperature detectors (PRTDs), embedded in the device, provides the corresponding freezing temperature. PRTD and microfluidic device fabrication methods are described in Appendix A and B, respectively.

In summary, this method forms the basis of a microfluidic approach for INP measurements on UAS: an ambient sample that contains INPs is collected into droplets within a microfluidic device, the droplets are cooled to near their freezing point, and the precise temperature at which the droplets freeze is measured with a PRTD array embedded on the device.

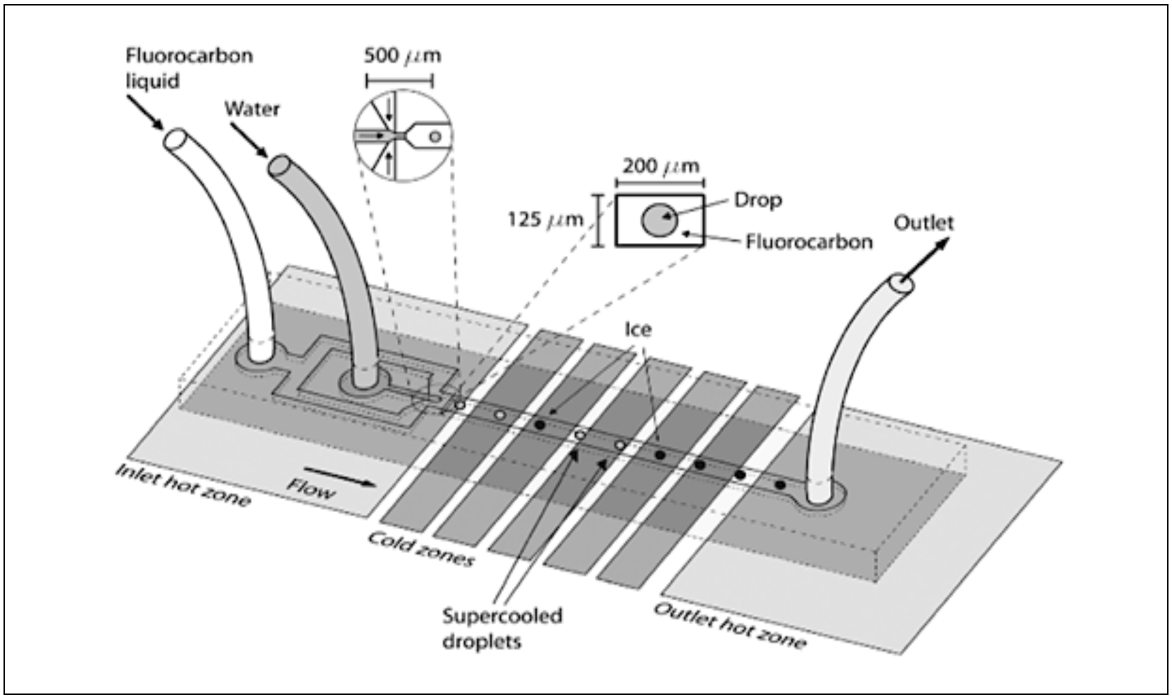

Figure 2. Schematic of the microfluidic platform on a cooling stage. Water droplets are carried from left to right over the cold stage. Figure from Stan et al. (2009).[2]

CHAPTER 2

Experiment Setup and Initial Experiments

The initial tests began with generating droplets using a pair of syringe pumps coupled to the PDMS microfluidic device using Teflon tubing. To attach the tubing to the device we removed a cylinder of PDMS material above the oil and water input regions of the device using a medical biopsy punch. The small size of the punch and flexibility of the PDMS materials guarantees a tight, seal by simply inserting the tubing into the PDMS. One pair of syringe pumps were used to see if desired droplet sizes (i.e. droplet diameter much smaller than the dimensions of the flow channel) can be achieved. However, experiments revealed that the smallest achievable droplets came into contact with the channel walls (Fig. 3). Moreover, we also observed that there was often a small amount of air which led to an inconsistent compression rate on the syringes, resulting in inconsistent droplet formation. To fix this inconsistency, we had to go through a trial-and-error process of changing the inlet flow rates until consistent droplet formation with desired droplet sizes was achieved. This process was time consuming and not desirable for a continuous INP measurement system. Therefore, in our later experiments, we used a pair of pressure pumps to force compressed air into the headspace of liquid reservoirs, thus pushing the liquids through the tubing with constant pressure rather than flow rate. This approach indicated a much easier way to generate a consistent series of monodisperse droplets using the pressure valves.

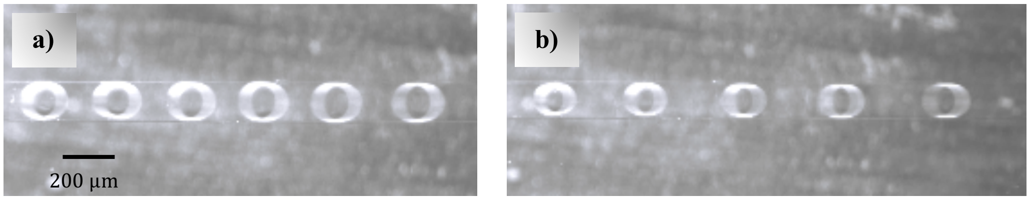

Figure 3. Water droplets in contact with the channel walls carried in mineral oil at $Q_{oil} = 0.4$ ml/h and $Q_{water} = 0.2$ ml/h (a) and 0.1 ml/h (b) at room temperature.

Fig. 4 shows the setup used for performing freezing experiments. Microfluidic device is mounted on the cold stage while pressure pumps push the continuous and dispersed phase into the device (Fig. 5). We used a chiller to decrease the temperature of a coolant fluid (ethanol) to around -15 °C. The coolant fluid is then pushed through a copper tubing to a bath of dry ice and acetone (Fig. 6) to further reduce its temperature to around -90 °C before being pushed into the cold stage (Fig. 7). Another chiller is used to keep the temperature of the droplet formation region at 25 °C to assure consistent droplet formation (Fig. 8a).

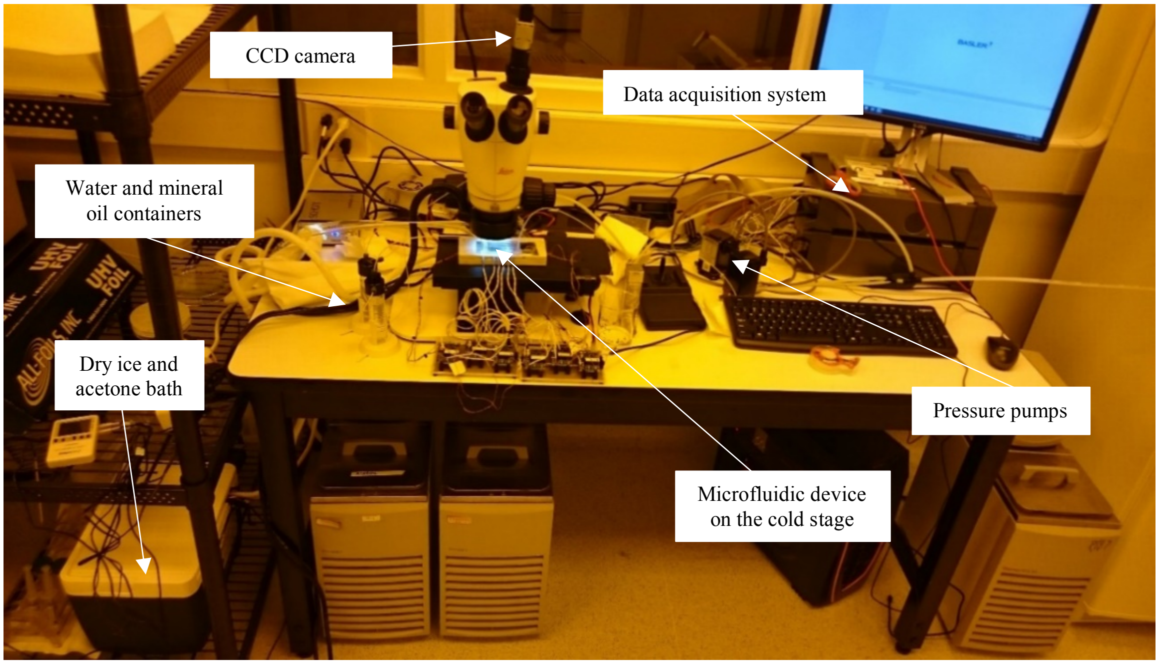

Figure 4. Photograph of experiment setup for the preliminary experiments in this project.

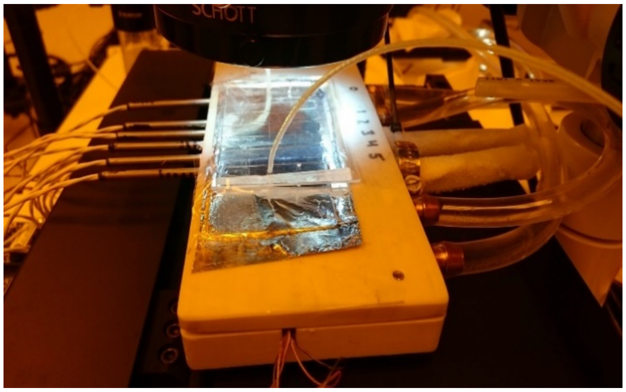

Figure 5. Closeup of the microfluidic device on the cold stage.

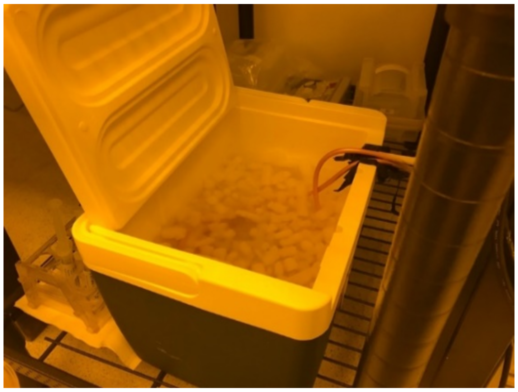

Figure 6. Bath of dry ice and acetone.

During the freezing experiments we noticed that droplet formation behavior changes when temperature of the cold stage changes significantly. This change leads to inconsistent droplet formation in which large slugs of the dispersed phase can be formed (Fig. 8b). These slugs are in contact with the channel wall and will block the channel when they freeze over the cold stage. Newly formed droplets also hit this ice block to the point that the entire channel was filled with frozen water (Fig. 9b). At this point, the experiment had to be stopped to either warm up the frozen microchannel or to substitute it with another microfluidic device.

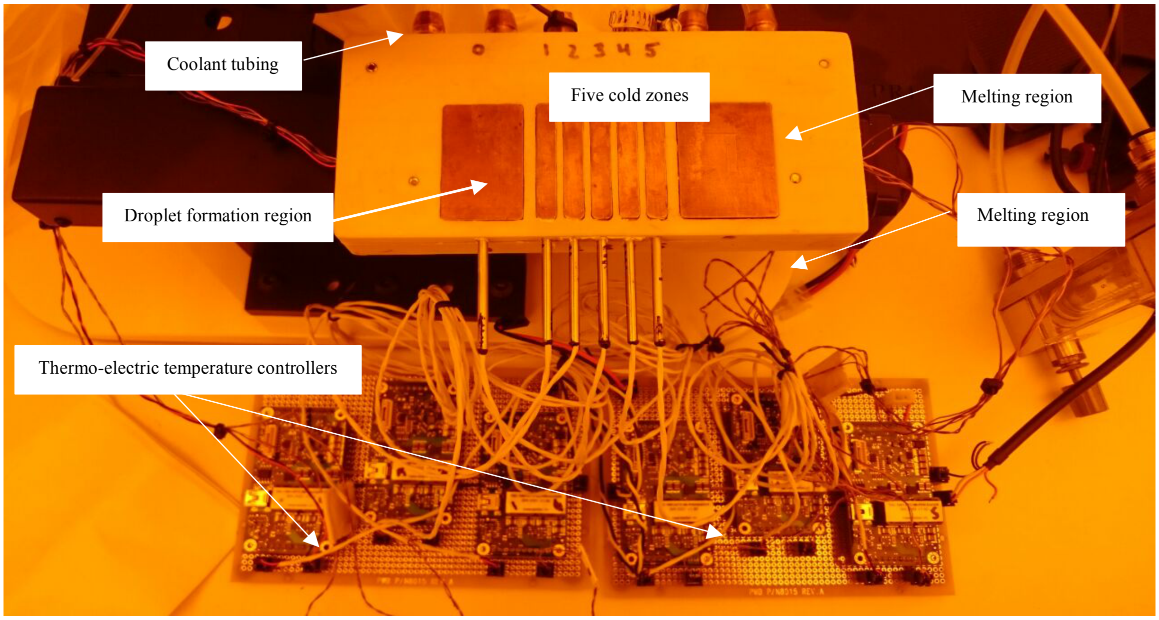

Figure 7. Photograph of cold stage and thermo-electric controllers used in this project.

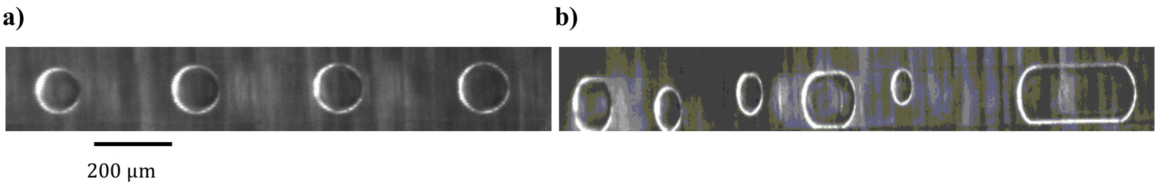

Figure 8. Consistent droplet formation (a) vs inconsistent droplet formation during the cooling process (b).

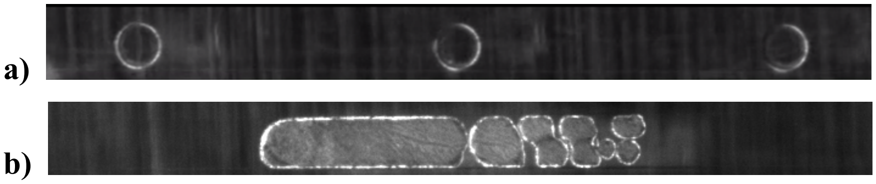

Figure 9. Images of experiments using Arizona Test Dust suspended in water. Top: liquid droplets traveling from left to right, fully suspended in the middle of the flow channel. Bottom: ice clogging the channel. ($T_{cold\ stage} = -20℃$)

Droplet generation and freezing experiments revealed several important challenges that must be overcome in the future development of this project. First, the INP measurement instrument must have an online method for assessing the consistency and quality of the droplet formation and have the capability to adjust input fluid flows to maintain a steady droplet generation rate. Second, one of the parameters that affects droplet formation is the cold stage temperature. Freezing temperatures at the cold zone increases the fluids' viscosities and results in higher pressure in the channel. We hypothesize that this pressure increase can affect the droplet formation region due to the elastic nature of PDMS.

In this study we have performed a series of 2D numerical simulations to establish the mathematical relations that describe the variety of droplet properties with respect to continuous phase flow rate in the INP measurement microfluidic device. Also, 3D numerical simulations are used to study the effect of external cooling on the pressure at the formation region. The results from this study provide insight into designing a continuous INP measurement instrument.

Fluid Dynamics Modeling

The numerical models in this study were implemented in Ansys Fluent 19.0 software package. The Volume of Fluid (VOF) interface capturing method available in the Fluent CFD solver has been used in a variety of numerical studies to investigate droplet formation and transport in different microfluidic geometries, including T-junction,[57] co-flowing,[58] and flow-focusing.[59]

Governing equations

The transient flow of liquids in the model is governed by the continuity and Navier-Stokes equations as follows.

Continuity equation:

$$\nabla \cdot (\rho\, \vec{U}) = 0 \tag{1}$$

Navier-stokes equation:

$$\frac{\partial(\rho\vec{U})}{\partial t} + \nabla \cdot \left(\rho\vec{U} \times \vec{U}\right) = -\nabla P + \nabla \cdot (\bar{\bar{\tau}}) + \rho\vec{g} + \vec{F} \tag{2}$$

In eq. 1 and eq. 2, $\vec{U}$, P, $\bar{\bar{\tau}}$, $\rho\vec{g}$, $\vec{F}$ are velocity vector, static pressure, shear tensor, gravitational body force, and external body forces, respectively. The interface between the fluid is tracked by solving continuity equation for each of the phases, as follows.

$$\frac{\partial\alpha_q}{\partial t} + \vec{U} \cdot \nabla\alpha_q = 0 \tag{3}$$

In eq. 3,α_q is the volume fraction of the phase q, where $\sum \alpha = 1$ for each computational cell in the domain and $0 \leq \alpha_q \leq 1$. When a cell is completely filled with phase q, $\alpha_q = 1$, whereas, $\alpha_q = 0$ shows that the cell is devoid of phase q.

The temperature of each cell of the model domain is calculated using the energy equation.

$$\frac{\partial}{\partial_t} + \nabla \cdot \left(\vec{v} \cdot (\rho E + P)\right) = \nabla \cdot (k_{eff} \nabla T) + S_h \tag{4}$$

In eq. 4, k_{eff} is effective thermal conductivity and S_h is the heat source term.[60]

Droplet size, frequency, and velocity analysis

As mentioned before, although manipulating the flow rate ratio is the most common method for achieving desired droplet size, generation frequency, and velocity, these parameters cannot be controlled independently. Each of these parameters is a function of flow rate ratio; thus, a system of three algebraic equations must be derived for a specific device geometry at constant dispersed phase flow rate. By solving the described system of equations, a three variable equation can be derived which shows the relationship between droplet size, frequency, and flow rate ratio. Therefore, the objectives of the numerical simulations in this section are:

- Study the effect of flow rate ratio on droplet size, generation frequency, and velocity in a flow-focusing microfluidic device.
- Derive equations that correlate flow rate ratio to droplet size, frequency, and velocity.

- Develop a mathematical equation that describes all the possible configurations of droplet size, generation frequency, and velocity for a specific dispersed phase flow rate.

Problem statement. A two-dimensional geometry of the flow-focusing microfluidic device used in our INP experiments is considered and the effect of flow rate ratio on size, velocity, and generation frequency is studied. The dispersed phase (water) is introduced through the main channel while the continuous phase (mineral oil) enters the device from the two symmetrical side channels. At the generation region where two phases meet, complex physical interactions between the two fluids result in the formation of a series of droplets.

Model setup. A rectangular 1 μm grid has been used in this study after performing a mesh independency test (Fig. 10) . The results showed that, when mesh size larger than 1.4 μm is used, the solver cannot track the interface of the forming droplets properly; therefore, the dispersed phase spreads on the throat wall of the device, which leads to an invalid numerical solution. Therefore, mesh sizes smaller than 1.4 μm are used in the mesh independency test and a 1 μm mesh face size was selected for each element in the computational domain. The continuous and dispersed phases enter the channel with a constant dispersed flow rate of $50\ \mu l/h$ and flow rate ratios, $\varphi = \frac{Q_c}{Q_d} = 2.5, 5, 7.5, 10, 12.5$. Table. 2 indicates the physical properties of both continuous and dispersed fluids. Constant inlet velocities for both the continuous and dispersed phases are specified, while atmospheric pressure boundary is imposed at the outlet. The continuous phase is assumed to wet the device walls completely before dispersed phase is introduced. Flow rate ratio is adjusted so that droplets are formed in the throat of device without spreading to the walls. The volume of fluid (VOF) method was used to trace the interface between the two phases. The pressure implicit with splitting of operators (PISO) algorithm was used for the pressure-velocity coupling,[61] while quadradic upstream interpolation for convective kinetics (QUICK) scheme was employed for solving the momentum equation.[62] The pressure interpolation was performed by pressure staggering option (PRESTO!) method.[63] The geometric reconstruction and second-order upwind schemes are adopted to solve the volume fraction and energy equations, respectively. A relatively short time step ($\mathrm{t} = 10^{-6}$ seconds) is specified to avoid inaccurate results (Fig. 11). Subsequently, constant Courant number ($\mathrm{Co} = 0.25$) is specified to solve the governing equations. The convergence criteria for continuity and momentum equations were set to 10^{-3} and 10^{-4}, respectively.

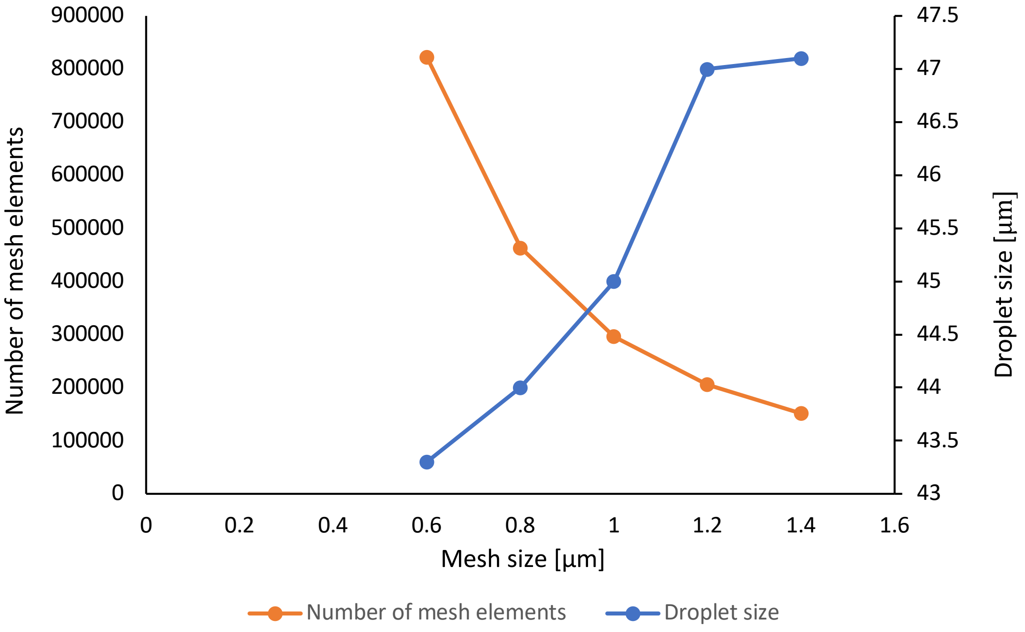

Figure 10. Mesh independency test.

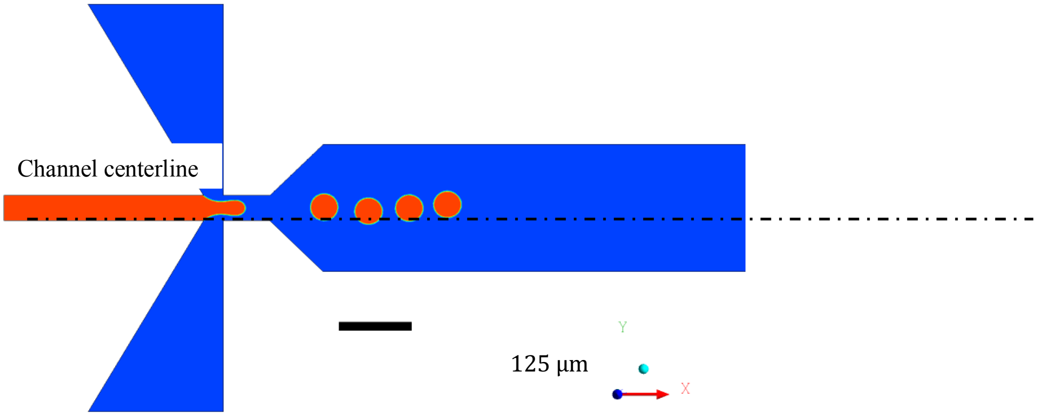

Figure 11. An example of inaccurate results when time step is set at 10^{-5} seconds. (Despite of symmetric boundary conditions, droplets do not travel on the centerline of the channel.)

Table 2. Physical properties of the continuous and dispersed phases used in the constant temperature simulations.[52,64] (T = 293.15 K)

Physical properties	**Continuous phase** (mineral oil)	**Dispersed phase** (water)
Density [kg/m^3]	848.7894	998.2
Viscosity [Pa· s]	0.0330	0.001003
Interfacial tension [N/m]	0.018685	

Effect of droplet size on time required for freezing

The heat transfer between the droplets and the cold stage are affected by droplets' volume and velocity, both of which are controlled by flow rate ratio. If we assume that temperature within the droplet remains uniform during the heat transfer, the lumped system method (eq. 5) can be used to estimate the time required for droplets to reach thermal equilibrium with the continuous phase.[52,65] The accuracy of this method depends on how close the uniform temperature assumption is to reality, which is determined by the Biot number.[65] The Biot number (eq. 6) is defined as the ratio of body's conduction resistance to convection resistance. The lumped system method is considered applicable when the condition $\mathrm{Bi} \leq 0.1$ is satisfied.[65]

$$\frac{\mathrm{T(t)} - \mathrm{T}_\infty}{\mathrm{T_i} - \mathrm{T}_\infty} = \mathrm{e}^{\left|\frac{\mathrm{hA}}{\rho_\mathrm{w} \forall \mathrm{C}_{\mathrm{p_w}}}\right|\mathrm{t}} \tag{5}$$

$$\mathrm{Bi} = \frac{\mathrm{hL_c}}{\mathrm{k_w}} \tag{6}$$

Where, $\mathrm{L_c} = \frac{\forall}{\mathrm{A}}$. In eq. 5, t is the time required by a water droplet at temperature $\mathrm{T(t)}$ to reach the steady state mineral oil temperature T_∞, from its initial temperature $\mathrm{T_i}$. ρ_w, $\mathrm{C}_{\mathrm{p_w}}$, and $\mathrm{k_w}$ are water density, specific heat ratio, and thermal conductivity, respectively. In eq. 6, $\mathrm{L_c}$ is characteristic length of a droplet, and A and ∀ are droplet surface area and volume, respectively. The heat transfer coefficient h is defined by eq. 7.

$$\mathrm{h} = \frac{\mathrm{k_o\ Nu}}{\mathrm{D_{Hy}}} \tag{7}$$

Where $\mathrm{D_{Hy}}$ is hydraulic diameter of the channel defined by eq. 8.

$$\mathrm{D_{Hy}} = \frac{2\mathrm{w.h}}{\mathrm{w+h}} \tag{8}$$

The Nusselt number (Nu) is defined using eq. 9.[66,67]

$$\mathrm{Nu} = 2 + 0.6\mathrm{Re}^{1/2}\mathrm{Pr}^{1/3} \tag{9}$$

The Prandtl number (Pr) and Reynolds number (Re) are defined by eq. 10 and eq. 11, respectively.

$$\mathrm{Pr} = \frac{\mu C_{p_o}}{k} \tag{10}$$

$$\mathrm{Re} = \frac{\rho_o u D_{Hy}}{\mu} \tag{11}$$

Where u is flow velocity; μ, ρ_o, and C_{p_o} are mineral oil viscosity, density, and specific heat, respectively. Table 3 shows the variable used in the analysis.

Table 3. List of variables used in the analysis.

$T(i)$	Droplet temperature [K]	$\forall$	Droplet volume [m^3]
T_∞	Oil temperature [K]	c_p	Specific heat [J/kg. K]
T_i	Droplet initial temperature	t	Time [s]
h	Heat transfer coefficient [W/m^2. K]	L_c	Characteristic length [m]
A	Droplet surface area [m^2]	k	Thermal conductivity [W/m. K]
ρ	Density [kg/m^3]	μ	Oil viscosity [Pa. s]
D_{Hy}	Hydraulic diameter of the channel [-]	u	Flow velocity [m/s]
w	Channel width [m]	h	Channel height [m]

Effect of cold stage temperature on the pressure inside the microfluidic device

Three-dimensional simulations are necessary to study droplet formation in response to downstream external cooling because the cold boundary cannot be specified in two-dimensional geometries. However, 3D simulations involving heat transfer are complicated and computationally expensive.[68] Moreover, the microfluidic device geometry used in this study has a relatively long (~5 cm) extended channel, which results in a large number of elements in the computational domain. To tackle this challenge, the simulations are divided into two less computationally demanding models as follows:

1. The effect of cold zone temperature on the pressure inside the channel is estimated using steady simulations. In the simulations only mineral oil is introduced at the inlets of the device.
2. Based on the results from the previous model, a pressure outlet boundary is set 1 mm downstream of the droplet formation region to represent the pressure increase in the channel caused by cooling (Fig. 12). Transient simulations are performed to study pressure changes in the channel during droplet formation.

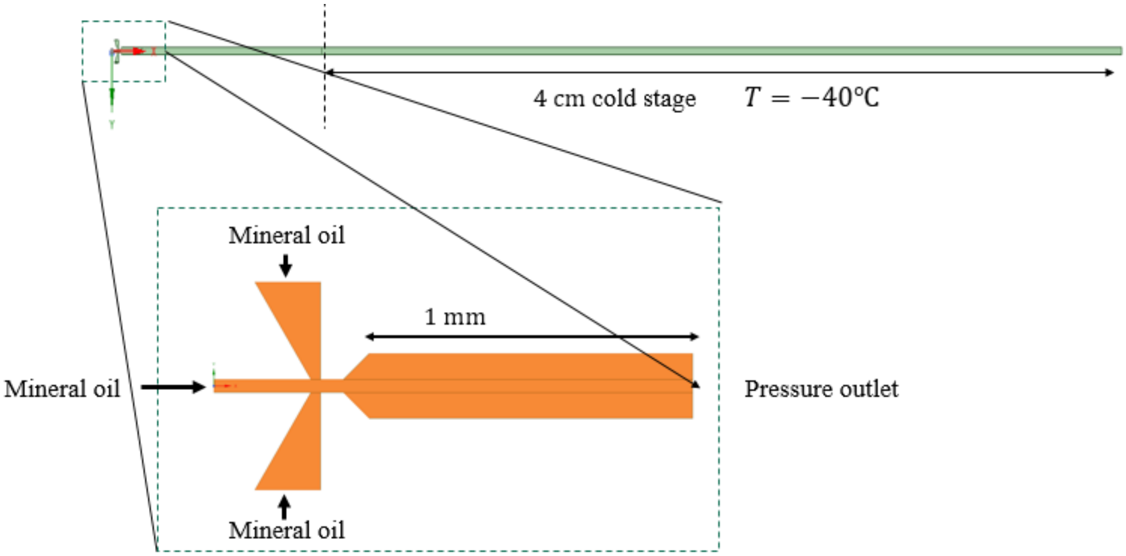

Figure 12. Schematic of the 3D simulation approach.

Problem 1 statement. A three-dimensional geometry of the flow-focusing microfluidic device with a 5 cm extended channel is considered as the domain for numerical simulations. There is a 4 cm cold zone 1 cm downstream of the droplet formation region. Mineral oil at constant flow rate and temperature is introduced at the inlets of the device and it is assumed to be in direct contact with the cold boundary. Numerical simulations have been performed to determine the steady state pressure at 1 mm downstream of the channel when two different temperatures ($\mathrm{T} = 25\ ^{\circ}\mathrm{C}$ and $\mathrm{T} = -40\ ^{\circ}\mathrm{C}$) are applied to the cold wall boundary.

Model 1 setup. A 5 mm mesh is used to divide the computational domain into 8,225,200 cubic elements. Cold zone temperature is considered to be $\mathrm{T} = 25\ ^{\circ}\mathrm{C}, 0\ ^{\circ}\mathrm{C}, -20\ ^{\circ}\mathrm{C}, -40\ ^{\circ}\mathrm{C}$ for each individual simulation. Constant flow rate and atmospheric pressure are imposed at the inlets and outlet, respectively. Temperature dependent properties of the mineral oil are shown in Table 3. The SIMPLE scheme was used for the pressure-velocity coupling in the continuity equation and pressure interpolation was performed by the Second Order method.[60] The Second Order Upwind method was used to solve the momentum and energy equation.[60] The convergence criteria for continuity, momentum, and energy equations were set to be 10^{-3}, 10^{-3}, and 10^{-6}; respectively.

Table 4. Physical properties of the mineral oil as function of temperature (T).[52,64]

Physical properties	**Mineral oil**
Density $[\mathrm{kg/m^3}]$	$-0.524\mathrm{T} + 1002.4$
Viscosity $[\mathrm{Pa.\,s}]$	$9 \times 10^{-6}\mathrm{T}^2 - 0.0061\mathrm{T} + 1.0478$
Thermal conductivity $[\mathrm{W/m.\,K}]$	0.14
Specific heat $[\mathrm{J/Kg.\,K}]$	2500

Problem 2 statement. The three-dimensional geometry of the flow focusing device and 1 mm downstream channel are considered to calculate the transient pressure across the device during droplet formation (Fig. 12). Mineral oil and water are introduced to the device to form the droplets under two different pressure outlet boundary conditions which reflect the effect of two different temperatures ($\mathrm{T} = 25\ ^\circ\mathrm{C}$ and $\mathrm{T} = -40\ ^\circ\mathrm{C}$) at the downstream cold zone.

Model 2 setup. A 0.0014 mm mesh is used to divide the computational domain into $10{,}732{,}573$ cubic elements. Constant flow rates and atmospheric pressure are imposed at the inlet and the outlet of the geometry, respectively. It is also assumed that the domain is filled with mineral oil before water is introduced. Governing equations are solved using the same methods represented in two-dimensional simulations. A fixed time step (10^{-5} seconds) and constant Courant number ($\mathrm{Co} = 0.25$) are considered in the simulations. The convergence criteria for continuity and momentum equations were set to 10^{-4}.

MODELING RESULTS

Droplet Size, Frequency, and Velocity Analysis

Two-dimensional numerical simulations were carried out to study the effect of flow rate ratio on droplet size, velocity, and generation frequency. Fig. 13 shows the variation of droplet size at five different flow rate ratios ($\varphi = 2.5$, $\varphi = 5$, $\varphi = 7.5$, and $\varphi = 10$) with constant dispersed phase flow rate ($50\ \mu l/h$) at $t = 2.5\ ms$. As shown in the figure, the increase in the flow rate ratio results in generation of more droplets with relatively smaller size. Fig. 14 shows the mathematical relation that describes the effect of flow ratio on droplet size and generation frequency. When the flow rate ratio is increased from 2.5 to 10, droplet diameter decreases from 53 μm to 34 μm (~36%); while droplet generation frequency increases from 70 Hz to 147 Hz (110% increase). As the continuous phase flow rate increases, the magnitude of the symmetrical shearing forces acting on the dispersed phase also increases. Therefore, droplets are formed faster; thus, droplet volume decreases.

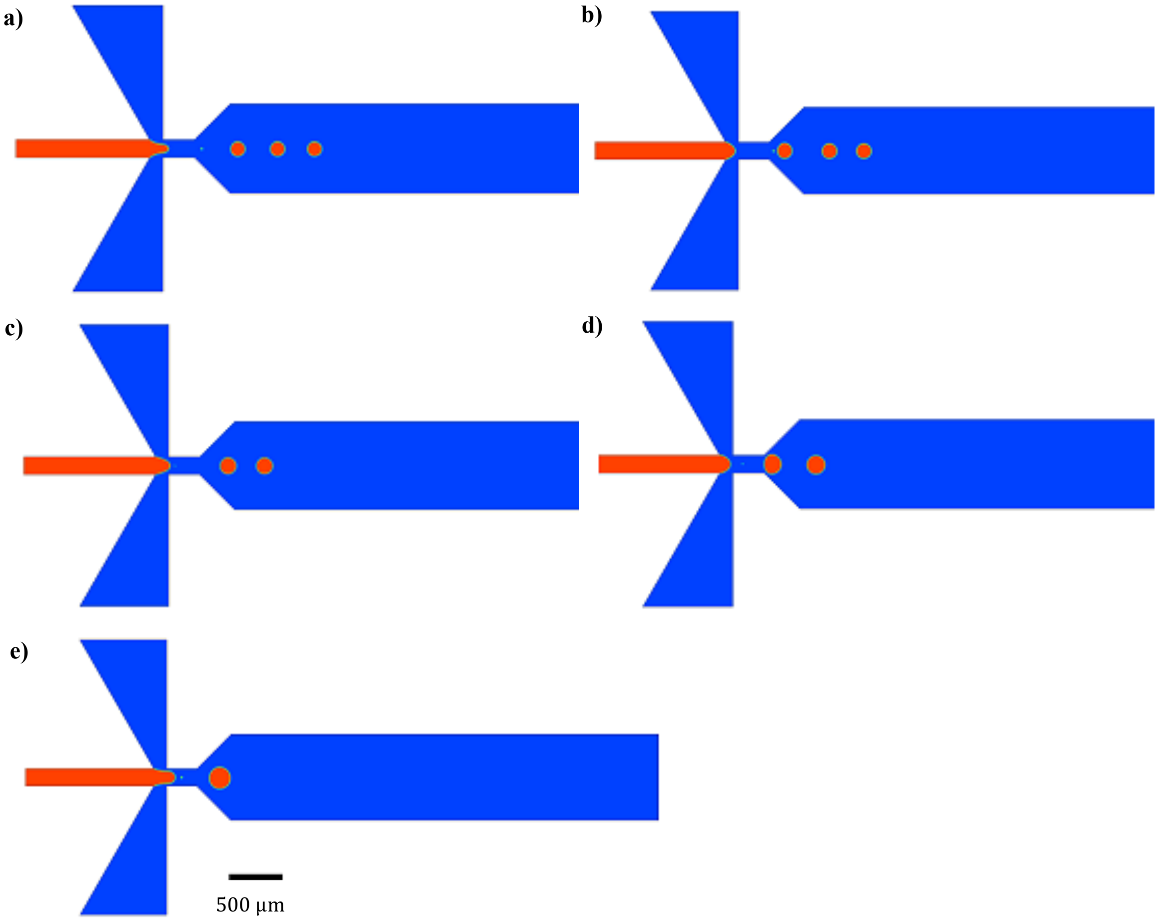

Figure 13. Water volume fraction at $t = 0.0025\ s$ and $Q_d = 50\ \mu l/h$ for the following flow rate ratios: (a) $\varphi = 2.5$. (b) $\varphi = 5$. (c) $\varphi = 7.5$. (d) $\varphi = 10$. (e) $\varphi = 12.5$.

Fig. 15 indicates that droplet velocity increases almost linearly from $3{,}933\ \mu\mathrm{m/s}$ at $\varphi = 2.5$, to $11{,}265\ \mu\mathrm{m/s}$ at $\varphi = 10$. As mentioned before, droplet velocity in the channel directly effects the reaction residence time in microfluidic systems; in our devices, droplet velocity effects the contact time with the cold zones in the microfluidic device. Based on the numerical results, it takes 3.55 seconds for the fastest droplets ($\varphi = 10$) to travel over the 4 cm cold stage in the experiments. Fig. 15. also shows that the distance between droplets increases linearly with the flow rate ratio. When flow rate ratio is increased from 2.5 to 10, distance between droplets increases from 4 μm to 42 μm. Therefore, at flow rate ratios smaller than 2.5, there is a high chance that droplets merge at the formation region of the channel. On the other hand, when the flow rate ratio is increased from 10 to 12.5, droplet size remains approximately constant ($d_{10} = 34.7$ and $d_{12.5} = 34.75$). Therefore, to reduce the computational time, $\varphi = 2.5$ and $\varphi = 10$ are considered the lower and upper limits of the flow rate ratio in this study, respectively. Within the introduced range, the following equations can be used to estimate droplet properties (diameter, generation frequency, and velocity) as a function of flow rate ratio.

$$\mathrm{d} = 69.74\varphi^{-0.3} \tag{12}$$

$$\mathrm{f} = 10.28\varphi + 47.5 \tag{13}$$

$$\mathrm{v} = 971.54\varphi + 1454.5 \tag{14}$$

Where d, f, and v are droplet diameter [μm], droplet frequency [Hz], and droplet velocity [μm/s]; Eq. 15 can be derived by combining the above equations as follows.

$$\left(\frac{d}{69.74}\right)^{-\frac{10}{3}} = \frac{1}{10.28}\ \mathrm{f} - 4.62 = \frac{1}{971.54}\ v - 1.49 \tag{15}$$

By knowing a desired droplet property (size, generation frequency, or velocity), eq. 15 can be used to determine the other two properties. This method can be used in future to design a droplet microfluidics chip that is capable of adjusting the flow rate at any time to achieve the desired droplet size, frequency, and velocity.

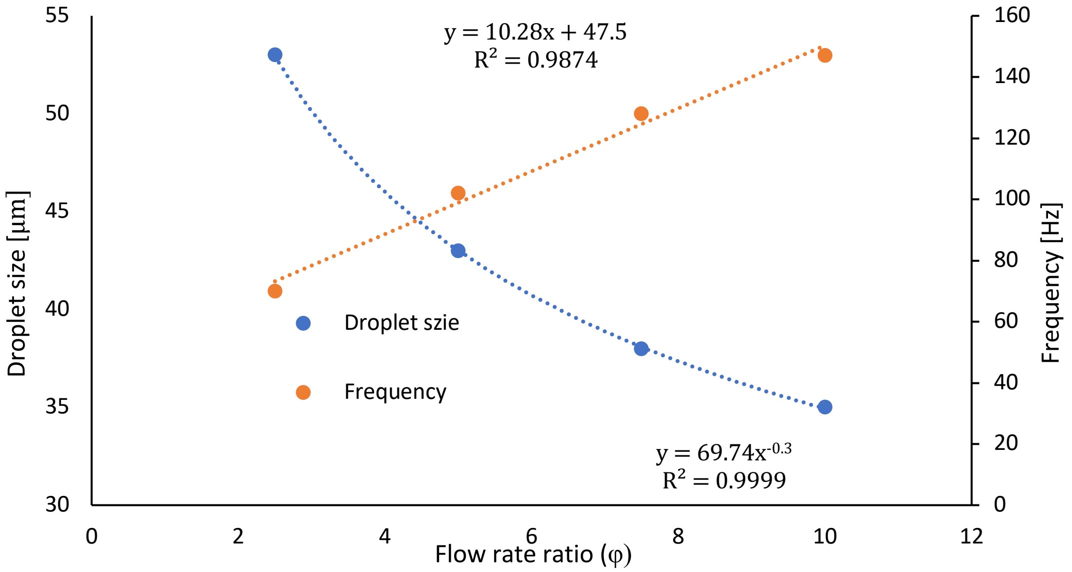

Figure 14. Variation of droplet diameter and droplet generation frequency with flow rate ratio.

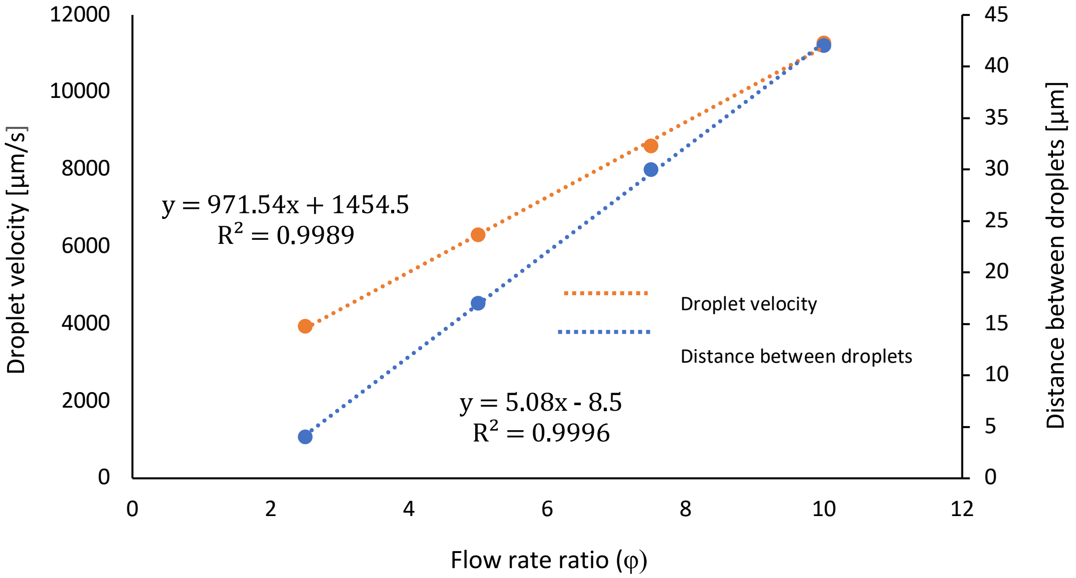

Figure 15. Variation of droplet velocity and distance between two consecutive droplets with flow rate ratio.

Fig. 16 shows a three-dimensional curve that describes the relationship between droplet properties and represents all the possible configurations of droplet size, frequency, and viscosity for the microfluidic device used in this research.

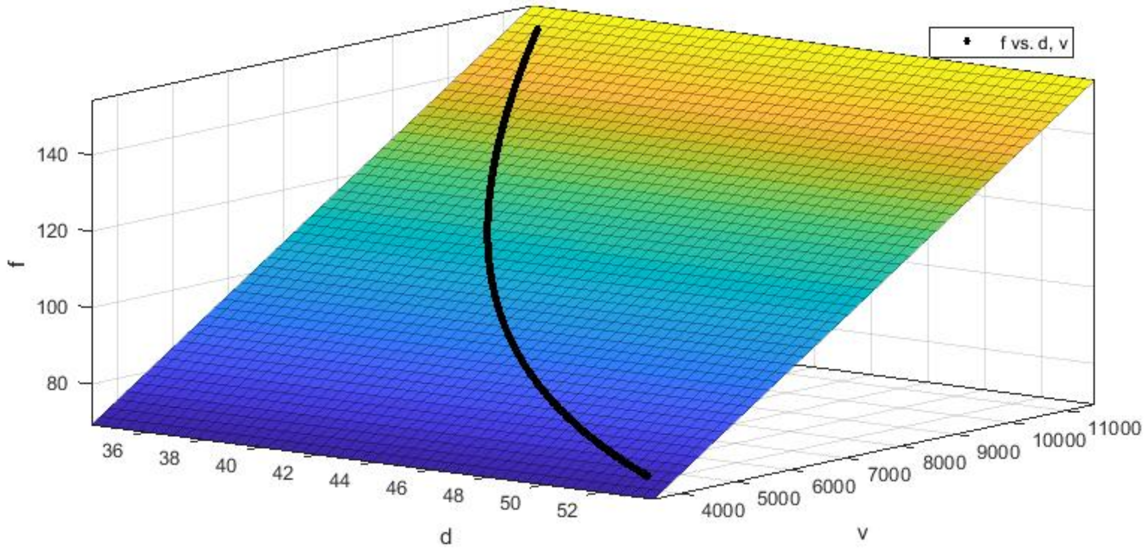

Figure 16. Black line represents possible configurations of droplet size, generation frequency, and velocity at $Q_d = 50\ \mu l/h$.

Lumped system analysis has been performed for four different sized droplets to determine the time that each droplet requires to reach $T_{droplet}$ = -39.9 °C; where cold stage temperature is considered to be at $T_{cold\ stage} = -40\ ℃$ (mathematically, droplet temperature reaches the temperature of the cold stage when t (time) approaches infinity) . Fig. 17 shows the variation of time required to cool down the entire droplet volume as a function of droplet diameter. Based on the results, when droplet dimeter changes from 35 μm to 53 μm, required cooling time increases from 47 ms to 82.3 ms (75%). Fig. 18 shows the temperature of the different sized droplets with respect to time during the cooling process. The smallest droplet reaches T = 39.9 ℃ after traveling 0.5 mm in silicon oil at T = −40 ℃. However, temperature of the silicon oil flowing over the cold stage is not uniform. Fig. 19 shows that silicon oil reaches the temperature of the cold stage after traveling 233.15 μm above the cold stage. Therefore, in a conservative redesign, the length of the cold stage can be reduced to around 1 cm.

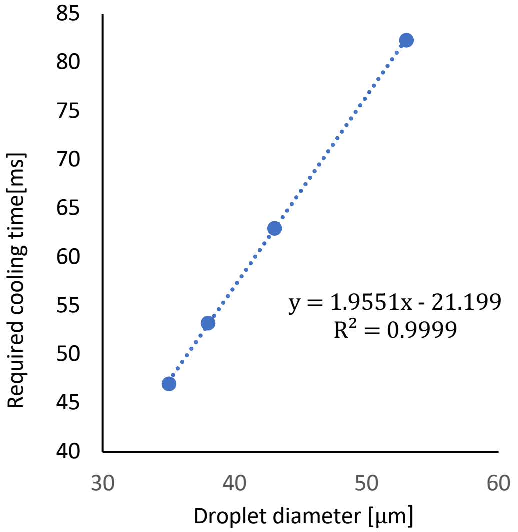

Figure 17. Variation of droplet diameter with required cooling time.

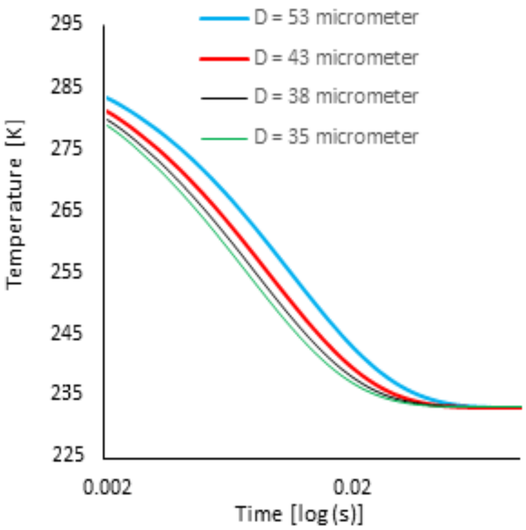

Figure 18. Variation of droplet temperature with time.

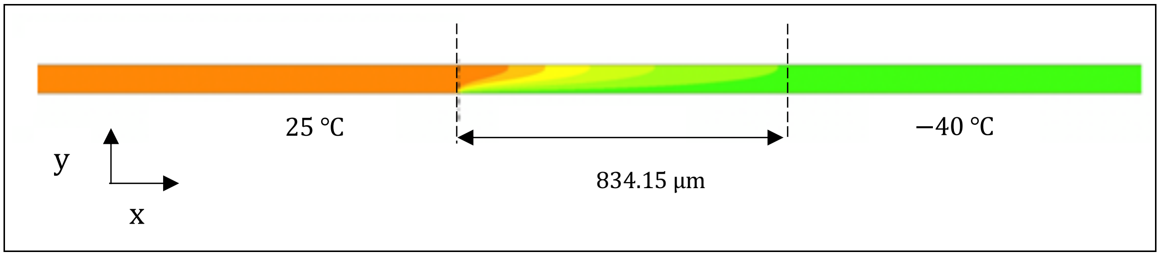

Figure 19. Temperature gradient at the XY plane of the channel (side view).

Effect of Downstream Cooling on the Pressure at the Droplet Formation Zone

Three-dimensional numerical simulations were performed to study the effect of the downstream cooling on the gauge pressure along the microfluidic geometry. Fig. 20 shows that the variation of pressure at the centerline of the channel at four different cold zone temperatures ($\mathrm{T} = 25\ °\mathrm{C}, \mathrm{T} = 0\ °\mathrm{C}, \mathrm{T} = 20\ °\mathrm{C}\ , \mathrm{T} = -40\ °\mathrm{C}$). When cold zone temperature is reduced from 25 °C to -40 °C, maximum steady-state pressure along the channel centerline increases from 46,000 Pa to 138,000 Pa, or by approximately 244%. Fig. 21 shows the correlation between cold zone temperature and channel maximum pressure.

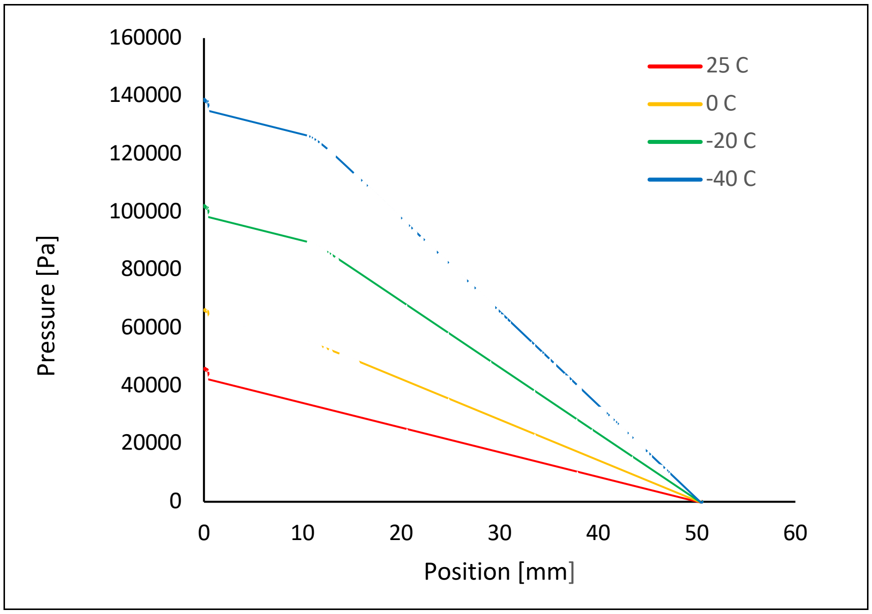

Figure 20. Modeled gauge pressure in the channel as a result of position and cold stage temperature. A position of 50 mm is the outlet boundary of the device, which is set to a gauge pressure of 0 Pa. ($Q_w = 110\ \mu l/h$ and $\varphi = 10$).

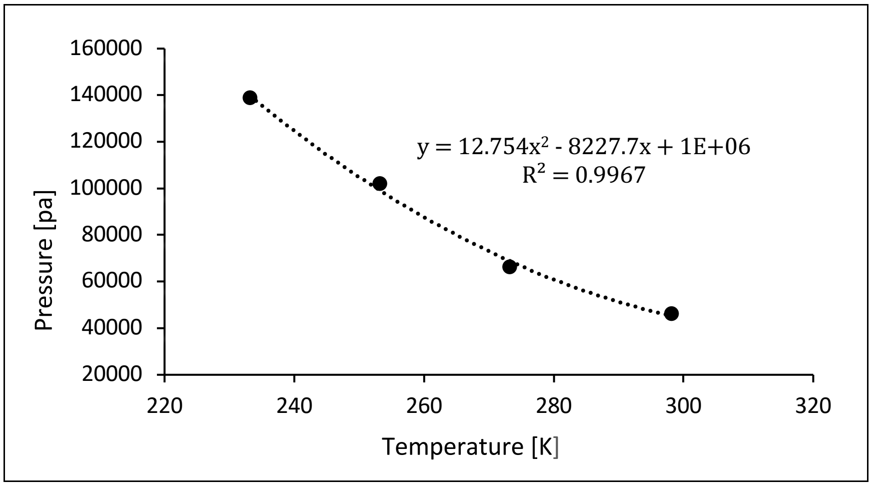

Figure 21. Variation of maximum pressure in the channel with cold zone temperature.

Because we were not sure the inlet flow rates used in above calculations lead to formation of a desirable-sized droplet, we readjusted inlet flow rates. In this case, water flow rate, and flow rate ratio (φ) are 100 μl/h and 15, respectively. In this case, pressure at 1 mm downstream of the channel increases from 37,252 Pa to 99,146 Pa (167%) when the cold zone temperature decreases from 25 °C to -40 °C. We used these pressures in three-dimensional multiphase simulations as outlet boundaries representing the effect of a downstream cold stage to calculate the maximum pressure in the channel during droplet formation.

Fig. 22 shows two slices of the channel at two different outlet pressures ($P = 37,252$ Pa and $P = 99,146.2$ Pa) at $t = 0.14$ s. These results show that droplet formation is not affected by the outlet boundary under the boundary conditions specified. Therefore, more parameters, including wall elasticity and heat transfer in the walls, need to be considered in numerical simulations. Fig. 23 shows the pressure at the centerline of the channel at $t = 0.14$ s and outlet pressure $P = 99,146.2$ Pa. Based on the results, the maximum pressure at the specified time is 102,784 Pa and occurs at the water inlet. This pressure is maintained nearly constant through the water inlet of the device and subsequently drops sharply at the junction with the continuous phase. Pressure inside each droplet is approximately 1300 Pa higher than the mineral oil stream surrounding it. Fig. 24 shows the pressure at the center point of the water inlet during a droplet formation cycle. Maximum pressure and minimum pressure during a droplet formation cycle are 102,350 Pa and 102,988 Pa; respectively. Pressure fluctuation due to droplet formation at the same point are less than 1% of the inlet pressure ($P = 102,755$ Pa).

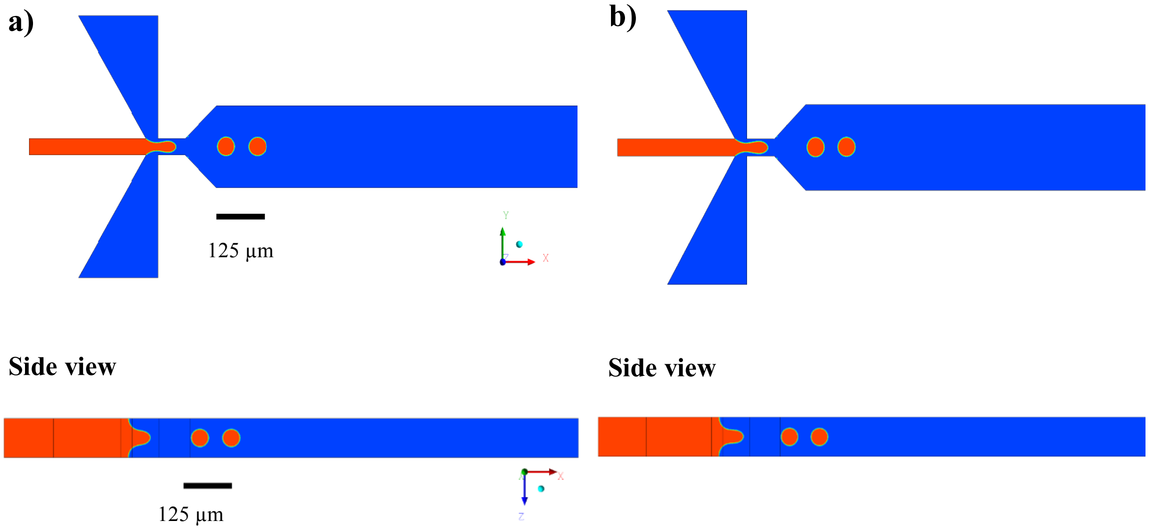

Figure 22. 3D Model results for drop formation. Water (in red) and silicone oil (in blue). Outlet pressure in (a) and (b) is 37,252 Pa and 99,146.2 *Pa*, respectively.

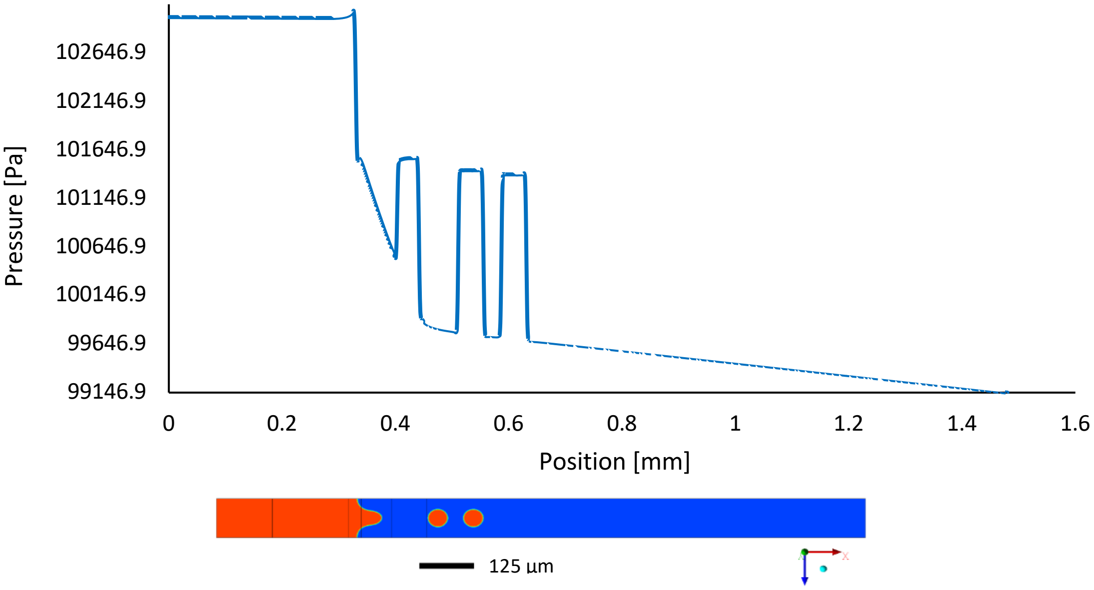

Figure 23. Pressure across the centerline of the channel when P = 99,246 Pa is applied as the outlet pressure.

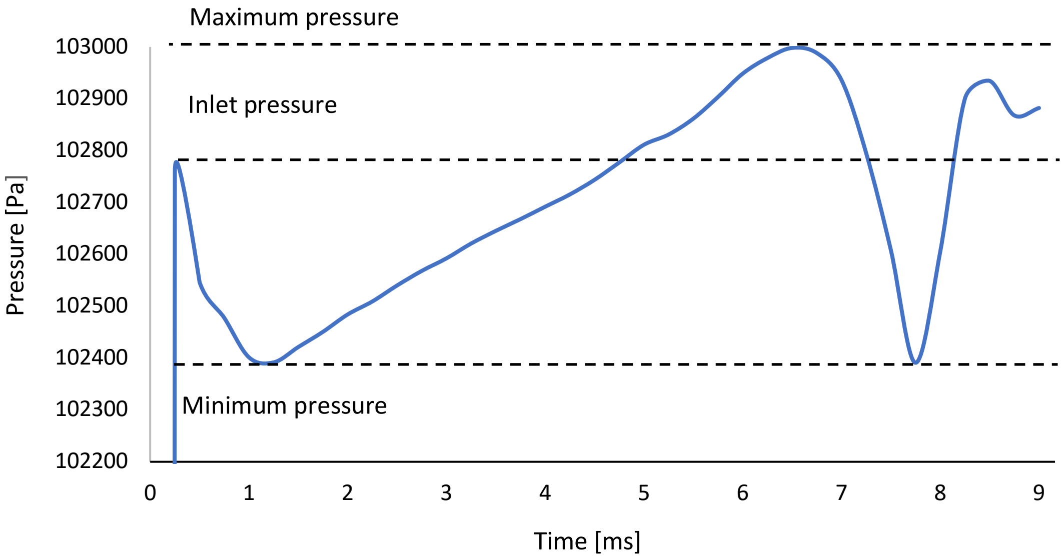

Figure 24. Variation of pressure at point x = 0, y = 0, and z = 50 µm (center point of the water inlet) with time during a droplet formation cycle.

CONCLUSION

The initial droplet generation and freezing experiments presented in this research revealed an important challenge that must be overcome in the future development of a continuous INP measurement instrument. The instrument must have an online method for assessing the consistency and quality of the droplet formation and have the capability to adjust input fluid flows to maintain a steady droplet generation rate. The online method requires knowledge of the relationship between droplet properties and flow rates. Therefore, two-dimensional numerical simulations were performed to establish the correlations among important droplet parameters, including droplet size, generation frequency, and velocity. These simulations showed that at a specific dispersed phase flow rate, droplet properties can only be defined within a specific range of the flow rate ratio. This range is specified by two limiting parameters: droplet size and distance between two subsequent droplets. Below a specific flow rate ratio, two subsequent droplets merge after droplet generation; while droplet size remains approximately constant above a specific flow rate ratio. This range for the microfluidic geometry used in this study $= [2.5,10]\ \mu l/h$ at a dispersed phase flow rate $Q_d = 50\ \mu l/h$. Four different flow rates ($Q_c = 2.5, 5, 7.5, 10$) $\mu l/h$ within this range were used in the simulations to establish the correlations that describe the droplet size, generation frequency, and velocity as a function of flow rate ratio. Moreover, the relationship among the droplet properties (droplet size, generation frequency, and velocity) was established. The derived relation represents a curve in the 3D cartesian coordinates system where droplet size, velocity, and frequency are the axis.

Downstream cooling in the microfluidic systems increases the viscosity of the fluids causing the pressure inside the channel to increase. In this study, three-dimensional numerical simulations suggested that pressure at $1\ \mathrm{mm}$ downstream of the formation zone increase by 167% when temperature of the cold stage is reduced from $25\ \mathrm{°C}$ to $-40\ \mathrm{°C}$. Pressure fluctuations at center point of the water inlet during a droplet formation cycle are less than 1% of the channel maximum pressure.

Lumped system analysis was performed to calculate the time that each droplet requires to reach the temperature of the cold stage. Based on the calculation, the largest droplet (d $= 53$ μm) can reach to 99.75% temperature of the cold stage after traveling approximately $1\ \mathrm{cm}$ above the cold stage. This method can be used in future cold stage designs in this project to optimize the cold stage size and reduce the effects of cooling on pressure in the channel.

FUTURE WORK

In this work we defined a limited range for the continuous phase flow rate at a constant dispersed phase flow rate and introduced a 3D curve that represents all possible configurations of droplet size, velocity, and generation frequency. For our specific device, future work needs to be done to find the continuous phase flow rate limits at different dispersed phase flow rates and to find the possible configurations of droplet properties within those ranges. By expanding to a more complete model, the future INP measurement device can switch between different flow rates to achieve desired droplet properties. By having enough data points, a 3D surface, unique to each flow-focusing microfluidic device, will govern the flow conditions necessary to produce desired droplet properties.

The transient pressure data on the channel walls calculated by the 3D simulations can be used in future numerical studies to study the effect of PDMS deformation on droplet behavior. Moreover, results from lumped analysis can be used in future simulations in which cold stage length is 1 cm. The reduction in the cold stage length decreases the number of mesh elements in the model domain, which leads to less computationally-intensive calculations, and therefore, modeling droplet formation and cooling processes at the same time can be performed faster.

APPENDICES

Appendix A: Microfluidic Device Fabrication

The fabrication process begins with rinsing and drying the glass wafers using the SRD (Spin Rinse Dryer) machine. Wafers are then soaked in a Nano-strip 2X (sulfuric acid 85%, hydrogen peroxide < 1%) solution at 65°C for 30 minutes, which is followed by careful rinsing and drying. To remove any moisture from the glass surface, wafers are baked at 200°C for 5 minutes. Wafers are then plasma-cleaned for two minutes (chamber pressure kept at 0.50 Torr) to remove any residual contamination from the glass surface.

A soft lithography technique (Fig. A1) is used to fabricate the microfluidic device. The lithography steps begin with spin-coating the glass surface with HMDS (hexamethyldisilizane) to improve the adhesion between the glass surface and the photoresist. The wafer is then spin-coated with uniform thickness (100 μm) of positive photoresist (SU-8 2100). Before exposure under UV light, the SU-8 coated wafer is baked for 5 minutes at 65°C followed by 20 minutes at 95°C. The wafer is then exposed under a UV source through the photomask (Fig. A2) which has the pattern of microfluidic flow channels to be fabricated. After post-exposure baking (5 minutes at 65° C followed by 20 minutes at 95° C), wafers are developed in PM-acetate which leaves the SU-8 pattern on the glass wafer in the transparent locations on the photomask. At this point, the wafer with patterned and cured SU-8 forms a master mold from which the PDMS devices can be made.

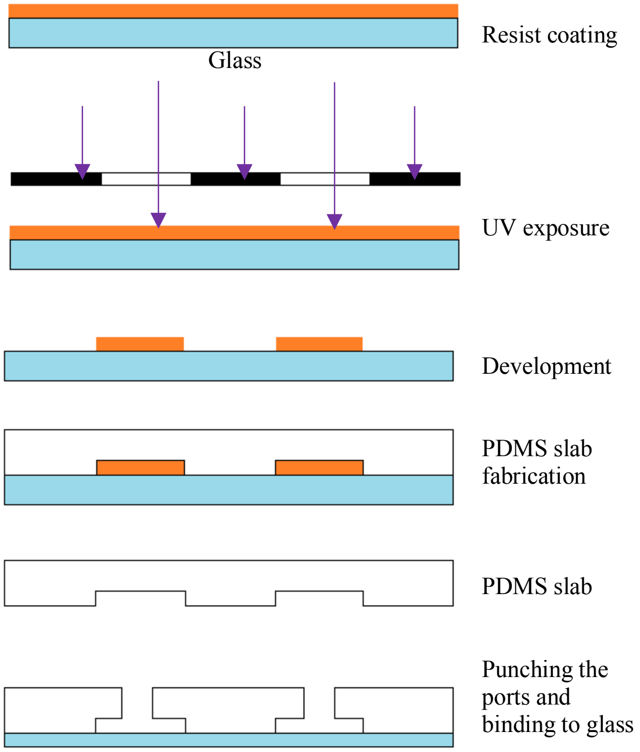

Figure A1. Soft lithography process, proceeding from top to bottom, for fabricating PDMS microfluidic devices. Figure adapted from Mazutis et al., 2013.[69]

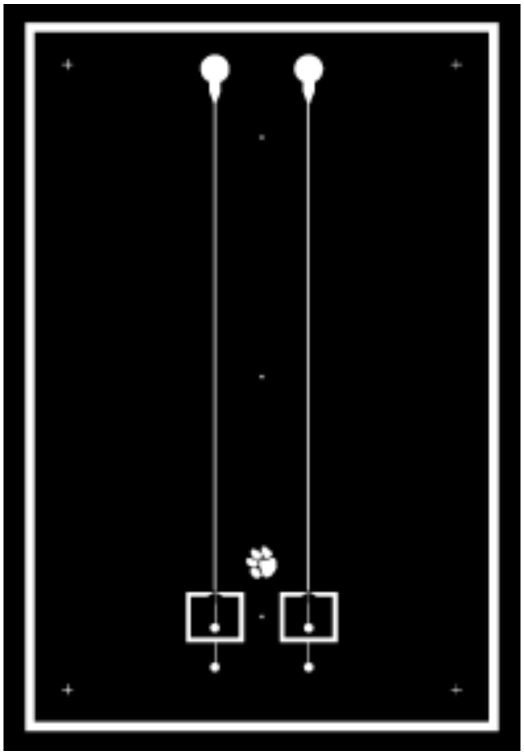

Figure A2. Photomask used to fabrication PDMS microfluidic flow channels.

To use the wafer mold, PDMS (Sylgard 184 Silicone Elastomer) is mixed at a 10:1 ratio of base curing agent and is poured over the wafer mold, which is first treated with a silane adhesion-inhibitor. Prior to curing in an oven, tiny air bubbles are removed from the PDMS in a vacuum desiccator held at low pressure for approximately 10 minutes. Any surface bubbles still stuck to the viscous PDMS are removed with a small flow of purified air to move the PDMS around to pop the bubbles. PDMS is cured by baking at about 70°C overnight. Finally, the PDMS slab containing the flow channels is cut out with a razor blade and holes are punched for the fluid delivery tubing. A complete list of the chemicals and equipment we use to fabricate the microfluidic devices can be found in Table A1.

Table A1. Materials and equipment used for microfluidic device fabrication.

Chemicals and Materials	**Equipment**
SU-8 Developer CAS number: 108-65-6	Plasma cleaner
Perfluorooctyltrichlorosilane CAS number: 78560-45-9	Spin coater
HDMS (hexamethyldisilane) CAS number: 999-97-3	UV lamp
SU-8 series resist	Hot plates
PDMS	Vacuum desiccator
Typical solvents (Acetone, methanol, etc.)	Oven

Appendix B: PRTD Fabrication and Initial Testing

The fabrication of PRTD (platinum resistance temperature detector) arrays took place in the Clemson Micro Fabrication Facility. The process, known as lift-off lithography and it is highly dependent on the tools available at specific clean room facilities. Fig. B1 shows an overview of the lift-off lithography process. Like soft-lithography described earlier, a photomask is used to pattern a photoresist onto glass wafers. To achieve the appropriate results, glass wafers must be cleaned in the same fashion described in Appendix A. After Nano-strip and plasma cleaning, the wafers are soaked in an adhesion promoter solution (surpass 300) for one minute to improve the adhesion between the glass surface and the photoresist. The wafers are then spin-coated with uniform thickness (0.9 µm) of a negative photoresist (AZ-5510) and baked at 110 °C for 105 seconds.

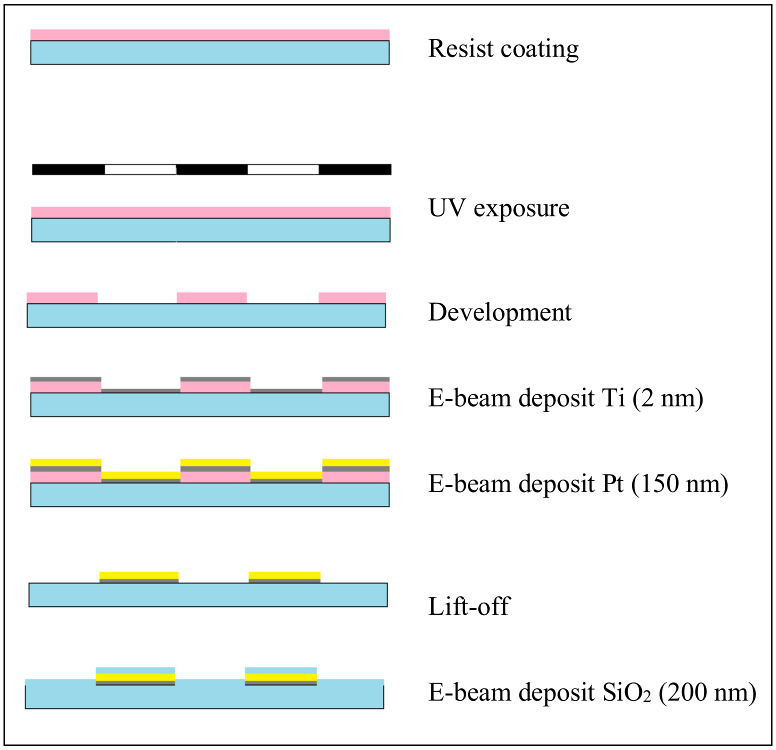

Fig. B1. Lift-off lithography process, proceeding from top to bottom, for fabricating PRTD arrays onto glass wafers. The final step indicates that the PRTD array device forms the glass slide used in the final PDMS microfluidic devices.

The PRTD array design is then patterned in the photoresist by UV exposure through a chrome mask using a mask aligner. The exposure time must be calculated each time based on the measured UV lamp intensity. After a short post-exposure bake, the printed PRTD array is developed to lift-off the resist from the areas that are not exposed by UV light; so that there is no photoresist on the area on which the metal will be deposited later. After inspection under a microscope, the wafers are plasma-etched for 30 seconds to remove any organic residue from their surface. Next, the wafers are loaded into an electron beam evaporator and ∼2 nm of titanium is deposited as an adhesion promoter between the glass and platinum. Platinum is then deposited to a thickness of ~150 nm. The platinum-coated wafers are then soaked in NMP (N-Methyl-2-pyrrolidone) in an ultrasonic tank to lift off the metal from the resist-coated areas and then cleaned in the SRD machine. Fabricated PRTD arrays (Fig. B2) are then annealed at ∼500 °C for ∼12 hours to lower the electrical resistance of the sensors. After another plasma cleaning, a ∼200 nm layer of SiO_2 is deposited on the PRTD arrays (except on the leads for electrical connection) to protect the sensors and prevent any fluid leakage when the final microfluidic device is assembled. The SiO_2 layer also provides a surface that can bond to PDMS. The fabrication process ends with cutting the PRTD arrays into a rectangular shape using wafer dicing saw. A complete list of the chemicals and equipment used for PRTD fabrication is listed in Table B1.

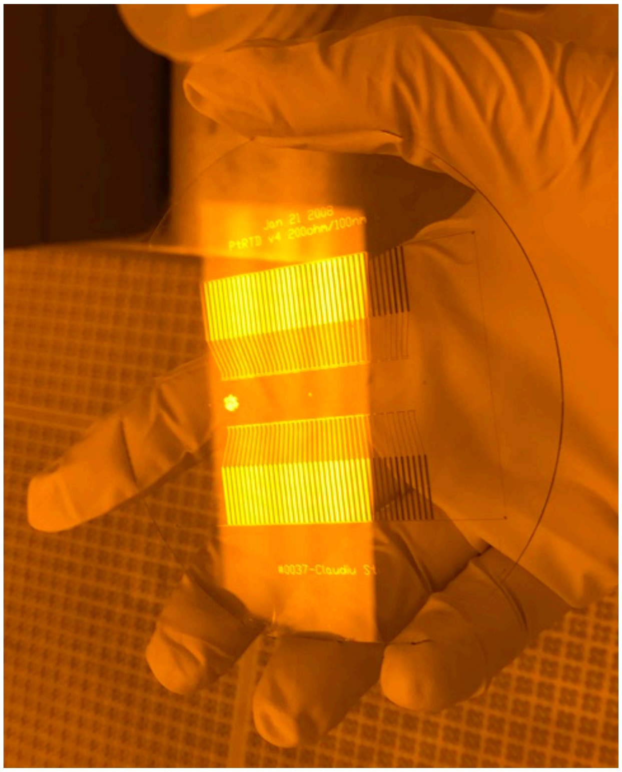

Fig. B2. Picture of a glass wafer with two PRTD array patterns deposited onto it.

Table B1. Materials and equipment used for PRTD fabrication.

Chemicals and Materials	Equipment
Nano-strip 2X (sulfuric acid 85%, hydrogen peroxide < 1%)	Profilometer (Tencore Alpha Step 200)
Glass wafers	Wafer holders
Adhesion Promoter (Surpass 300)	Hot plate
AZ-5510 Photoresist	Plasma etch (PlasmaTherm Versaline ICP)
Titanium CAS number: 7440-32-6	Spin coater (Brewer Sciences)
Platinum CAS number: 7440-06-4	Contact printer (Nuetronix/Quintel Q-7000-IR)
NMP (N-Methyl-2-pyrrolidone) CAS number: 872-50-4	Developer tool (Brewer Sciences)
Typical solvents (acetone, methanol, etc.)	Electron beam evaporator (CCS CA-40)

Chemicals and Materials	**Equipment**
MIF developer (AZ 300)	Ultrasonic tank
PGMEA (Propylene glycol methyl ether acetate) CAS number: 108-65-6	Microscope (Nikon Optical microscope magnification to 1500X)
Silicon dioxide CAS number: 7631-86-9	High temperature furnace
AZ-7710 Photoresist	Wafer dicing saw (K&S 780)

Appendix C: Study Data Storage

The numerical simulations presented in this study are stored in the following folders in the Clemson Air Quality Lab google drive.

Initial droplet formation models:

These initial models were performed to understand how proper settings must be set in the models to lead to valid results.

Address: G:\My Drive\MAML\Members\Ali\CFD\Paper data\Initial droplet formation models.

Mesh independency test:

These models were performed to find the appropriate mesh size for the simulations.

Address: G:\My Drive\MAML\Members\Ali\CFD\Paper data\Mesh test

Two-dimensional models for droplet formation:

These simulations were performed to determine droplet properties a function of flow rate ratio.

Address: G:\My Drive\MAML\Members\Ali\CFD\Paper data\Droplet formation\2D

Steady-state three dimensional models for effect of cold stage temperature on pressure:

These simulations provide the steady state pressure in the channel as the result of cooling. The results from this model is used in the following 3D models to investigate the effect of cooling on droplet formation.

Address: G:\My Drive\MAML\Members\Ali\CFD\Paper data\Steady-state pressure

Three-dimensional droplet formation:

Address: G:\My Drive\MAML\Members\Ali\CFD\Paper data\Droplet formation\3D

REFERENCES

(1) Debenedetti, P. G. *Metastable Liquids: Concepts and Principles*; Physical Chemistry: Science and Engineering; Princeton University Press, 1996.

(2) Stan, C. A.; Schneider, G. F.; Shevkoplyas, S. S.; Hashimoto, M.; Ibanescu, M.; Wiley, B. J.; Whitesides, G. M. A microfluidic apparatus for the study of ice nucleation in supercooled water drops. *Lab Chip* **2009**, *9* (16), 2293–2305.

(3) Moore, E. B.; Molinero, V. Structural transformation in supercooled water controls the crystallization rate of ice. *Nature* **2011**, *479* (7374), 506–508.

(4) Vali, G.; DeMott, P. J.; Möhler, O.; Whale, T. F. Technical Note: A proposal for ice nucleation terminology. *Atmos. Chem. Phys.* **2015**, *15* (18), 10263–10270.

(5) DeMott, P. J.; Prenni, A. J.; Liu, X.; Kreidenweis, S. M.; Petters, M. D.; Twohy, C. H.; Richardson, M. S.; Eidhammer, T.; Rogers, D. C. Predicting global atmospheric ice nuclei distributions and their impacts on climate. *Proc. Natl. Acad. Sci.* **2010**, *107* (25), 11217 LP–11222.

(6) Janjua, Z. A.; Turnbull, B.; Hibberd, S.; Choi, K.-S. Mixed ice accretion on aircraft wings. *Phys. Fluids* **2018**, *30* (2), 27101.

(7) Cheng, L.; Sun, D.-W.; Zhu, Z.; Zhang, Z. Emerging techniques for assisting and accelerating food freezing processes: A review of recent research progresses. *Crit. Rev. Food Sci. Nutr.* **2017**, *57* (4), 769–781.

(8) Oddone, I.; Barresi, A. A.; Pisano, R. Influence of controlled ice nucleation on the freeze-drying of pharmaceutical products: the secondary drying step. *Int. J. Pharm.* **2017**, *524* (1), 134–140.

(9) Neethirajan, S.; Kobayashi, I.; Nakajima, M.; Wu, D.; Nandagopal, S.; Lin, F. Microfluidics for food, agriculture and biosystems industries. *Lab Chip* **2011**, *11* (9), 1574–1586.

(10) John Morris, G.; Acton, E. Controlled ice nucleation in cryopreservation – A review. *Cryobiology* **2013**, *66* (2), 85–92.

(11) Clarke, A.; Morris, G. J.; Fonseca, F.; Murray, B. J.; Acton, E.; Price, H. C. A Low Temperature Limit for Life on Earth. *PLoS One* **2013**, *8* (6), e66207.

(12) Cantrell, W.; Heymsfield, A. Production of Ice in Tropospheric Clouds: A Review. *Bull. Am. Meteorol. Soc.* **2005**, *86* (6), 795–808.

(13) Kanji, Z. A.; Ladino, L. A.; Wex, H.; Boose, Y.; Burkert-Kohn, M.; Cziczo, D. J.; Krämer, M. Overview of Ice Nucleating Particles. *Meteorol. Monogr.* **2017**, *58*, 1.1–1.33.

(14) Abbatt, J. P. D. Interactions of Atmospheric Trace Gases with Ice Surfaces: Adsorption and Reaction. *Chem. Rev.* **2003**, *103* (12), 4783–4800.

(15) Murray, B. J.; Broadley, S. L.; Wilson, T. W.; Atkinson, J. D.; Wills, R. H. Heterogeneous freezing of water droplets containing kaolinite particles. *Atmos. Chem. Phys.* **2011**, *11* (9), 4191–4207.

(16) Prenni, A. J.; Harrington, J. Y.; Tjernström, M.; DeMott, P. J.; Avramov, A.; Long, C. N.; Kreidenweis, S. M.; Olsson, P. Q.; Verlinde, J. Can Ice-Nucleating Aerosols Affect Arctic Seasonal Climate? *Bull. Am. Meteorol. Soc.* **2007**, *88* (4), 541–550.

(17) Schrod, J.; Weber, D.; Drücke, J.; Keleshis, C.; Pikridas, M.; Ebert, M.; Cvetković, B.; Nickovic, S.; Marinou, E.; Baars, H.; et al. Ice nucleating particles over the Eastern Mediterranean measured by unmanned aircraft systems. *Atmos. Chem. Phys.* **2017**, *17* (7), 4817–4835.

(18) Rogers, D. C.; DeMott, P. J.; Kreidenweis, S. M.; Chen, Y. A continuous-flow diffusion chamber for airborne measurements of ice nuclei. *J. Atmos. Ocean. Technol.* **2001**, *18* (5), 725–741.

(19) Seinfeld, J. H.; Bretherton, C.; Carslaw, K. S.; Coe, H.; DeMott, P. J.; Dunlea, E. J.; Feingold, G.; Ghan, S.; Guenther, A. B.; Kahn, R.; et al. Improving our fundamental understanding of the role of aerosol−cloud interactions in the climate system. *Proc. Natl. Acad. Sci.* **2016**, *113* (21), 5781 LP – 5790.

(20) Le, H. P. Progress and trends in ink-jet printing technology. *J. Imaging Sci. Technol.* **1998**, *42* (1), 49–62.

(21) Terry, S. C.; Jerman, J. H.; Angell, J. B. A gas chromatographic air analyzer fabricated on a silicon wafer. *IEEE Trans. Electron Devices* **1979**, *26* (12), 1880–1886.

(22) Whitesides, G. M. The origins and the future of microfluidics. *Nature* **2006**, *442* (7101), 368–373.

(23) Effenhauser, C. S.; Paulus, A.; Manz, A.; Widmer, H. M. High-speed separation of antisense oligonucleotides on a micromachined capillary electrophoresis device. *Anal. Chem.* **1994**, *66* (18), 2949–2953.

(24) Woolley, A. T.; Mathies, R. A. Ultra-high-speed DNA fragment separations using microfabricated capillary array electrophoresis chips. *Proc. Natl. Acad. Sci.* **1994**, *91* (24), 11348–11352.

(25) Zilionis, R.; Nainys, J.; Veres, A.; Savova, V.; Zemmour, D.; Klein, A. M.; Mazutis, L. Single-cell barcoding and sequencing using droplet microfluidics. *Nat. Protoc.* **2016**, *12*, 44.

(26) Schneider, G. Automating drug discovery. *Nat. Rev. Drug Discov.* **2017**, *17*, 97.

(27) Bruijns, B. B.; Costantini, F.; Lovecchio, N.; Tiggelaar, R. M.; Di Timoteo, G.; Nascetti, A.; de Cesare, G.; Gardeniers, J. G. E.; Caputo, D. On-chip real-time monitoring of multiple displacement amplification of DNA. *Sensors Actuators B Chem.* **2019**, *293*, 16–22.

(28) Hassoun, M.; Rüger, J.; Kirchberger-Tolstik, T.; Schie, I. W.; Henkel, T.; Weber, K.; Cialla-May, D.; Krafft, C.; Popp, J. A droplet-based microfluidic chip as a platform for leukemia cell lysate identification using surface-enhanced Raman scattering. *Anal. Bioanal. Chem.* **2018**, *410* (3), 999–1006.

(29) Metcalf, A. R.; Narayan, S.; Dutcher, C. S. A review of microfluidic concepts and applications for atmospheric aerosol science. *Aerosol Sci. Technol.* **2018**, *52* (3), 310–329.

(30) Atencia, J.; Beebe, D. J. Controlled microfluidic interfaces. *Nature* **2005**, *437* (7059), 648–655.

(31) Thorsen, T.; Roberts, R. W.; Arnold, F. H.; Quake, S. R. Dynamic pattern formation in a vesicle-generating microfluidic device. *Phys. Rev. Lett.* **2001**, *86* (18), 4163.

(32) Yang, C.-G.; Xu, Z.-R.; Wang, J.-H. Manipulation of droplets in microfluidic systems. *TrAC Trends Anal. Chem.* **2010**, *29* (2), 141–157.

(33) Anna, S. L.; Bontoux, N.; Stone, H. A. Formation of dispersions using "flow focusing" in microchannels. *Appl. Phys. Lett.* **2003**, *82* (3), 364–366.

(34) Cramer, C.; Fischer, P.; Windhab, E. J. Drop formation in a co-flowing ambient fluid. *Chem. Eng. Sci.* **2004**, *59* (15), 3045–3058.

(35) Baroud, C. N.; Gallaire, F.; Dangla, R. Dynamics of microfluidic droplets. *Lab Chip* **2010**, *10* (16), 2032–2045.

(36) Ma, J.; Wang, Y.; Liu, J. Biomaterials meet microfluidics: from synthesis technologies to biological applications. *Micromachines* **2017**, *8* (8), 255.

(37) Kobayashi, I.; Uemura, K.; Nakajima, M. Formulation of monodisperse emulsions using submicron-channel arrays. *Colloids Surfaces A Physicochem. Eng. Asp.* **2007**, *296* (1), 285–289.

(38) Teh, S.-Y.; Lin, R.; Hung, L.-H.; Lee, A. P. Droplet microfluidics. *Lab Chip* **2008**, *8* (2), 198–220.

(39) Lan, W.; Li, S.; Luo, G. Numerical and experimental investigation of dripping and jetting flow in a coaxial micro-channel. *Chem. Eng. Sci.* **2015**, *134*, 76–85.

(40) Tan, S.; Murshed, S. M. S.; Nguyen, N. Thermally controlled droplet formation in flow focusing geometry : formation regimes and effect of nanoparticle. **2008**.

(41) Jamalabadi, M. Y. A.; DaqiqShirazi, M.; Kosar, A.; Shadloo, M. S. Effect of injection angle, density ratio, and viscosity on droplet formation in a microfluidic T-junction. *Theor. Appl. Mech. Lett.* **2017**, *7* (4), 243–251.

(42) Wehking, J. D.; Gabany, M.; Chew, L.; Kumar, R. Effects of viscosity, interfacial tension, and flow geometry on droplet formation in a microfluidic T-junction. *Microfluid. Nanofluidics* **2014**, *16* (3), 441–453.

(43) Sohel Murshed, S. M.; Tan, S.-H.; Nguyen, N.-T. Temperature dependence of interfacial properties and viscosity of nanofluids for droplet-based microfluidics. *J. Phys. D. Appl. Phys.* **2008**, *41* (8), 85502.

(44) Han, X.-W.; Zhang, H.-W.; Luo, H.-Y.; Zheng, X.-L.; Yang, Z.; Hu, N.; Liao, Y.-J.; Yang, J. Preparation of Poly(vinyl alcohol) Microspheres Based on Droplet Microfluidic Technology. *Chinese J. Anal. Chem.* **2018**, *46* (8), 1269–1274.

(45) Zhao, G.; Fu, J. Microfluidics for cryopreservation. *Biotechnol. Adv.* **2017**, *35* (2), 323–336.

(46) Park, J.; Jung, J. H.; Destgeer, G.; Ahmed, H.; Park, K.; Sung, H. J. Acoustothermal tweezer for droplet sorting in a disposable microfluidic chip. *Lab Chip* **2017**, *17* (6), 1031–1040.

(47) Lee, D.; Fang, C.; Ravan, A. S.; Fuller, G. G.; Shen, A. Q. Temperature controlled tensiometry using droplet microfluidics. *Lab Chip* **2017**, *17* (4), 717–726.

(48) Ting, T. H.; Yap, Y. F.; Nguyen, N.-T.; Wong, T. N.; Chai, J. C. K.; Yobas, L. Thermally mediated breakup of drops in microchannels. *Appl. Phys. Lett.* **2006**, *89* (23), 234101.

(49) Baroud, C. N.; Delville, J.-P.; Gallaire, F.; Wunenburger, R. Thermocapillary valve for droplet production and sorting. *Phys. Rev. E* **2007**, *75* (4), 46302.

(50) Yesiloz, G.; Boybay, M. S.; Ren, C. L. Effective Thermo-Capillary Mixing in Droplet Microfluidics Integrated with a Microwave Heater. *Anal. Chem.* **2017**, *89* (3), 1978–1984.

(51) Hong, Y.; Wang, F. Flow rate effect on droplet control in a co-flowing microfluidic device. *Microfluid. Nanofluidics* **2007**, *3* (3), 341–346.

(52) Khater, A.; Mohammadi, M.; Mohamad, A.; Nezhad, A. S. Dynamics of temperature-actuated droplets within microfluidics. *Sci. Rep.* **2019**, *9* (1), 3832.

(53) Laval, P.; Crombez, A.; Salmon, J.-B. Microfluidic Droplet Method for Nucleation Kinetics Measurements. *Langmuir* **2009**, *25* (3), 1836–1841.

(54) Teychené, S.; Biscans, B. Crystal nucleation in a droplet based microfluidic crystallizer. *Chem. Eng. Sci.* **2012**, *77*, 242–248.

(55) DeMott, P. J.; Möhler, O.; Stetzer, O.; Vali, G.; Levin, Z.; Petters, M. D.; Murakami, M.; Leisner, T.; Bundke, U.; Klein, H.; et al. Resurgence in Ice Nuclei Measurement Research. *Bull. Am. Meteorol. Soc.* **2011**, *92* (12), 1623–1635.

(56) Cziczo, D. J.; Ladino, L.; Boose, Y.; Kanji, Z. A.; Kupiszewski, P.; Lance, S.; Mertes, S.; Wex, H. Measurements of Ice Nucleating Particles and Ice Residuals. *Meteorol. Monogr.* **2016**, *58*, 8.1–8.13.

(57) Nekouei, M.; Vanapalli, S. A. Volume-of-fluid simulations in microfluidic T-junction devices: Influence of viscosity ratio on droplet size. *Phys. Fluids* **2017**, *29* (3), 32007.

(58) Deng, C.; Wang, H.; Huang, W.; Cheng, S. Numerical and experimental study of oil-in-water (O/W) droplet formation in a co-flowing capillary device. *Colloids Surfaces A Physicochem. Eng. Asp.* **2017**, *533*, 1–8.

(59) Li, Y.; Yamane, D. G.; Li, S.; Biswas, S.; Reddy, R. K.; Goettert, J. S.; Nandakumar, K.; Kumar, C. S. S. R. Geometric optimization of liquid–liquid slug flow in a flow-focusing millifluidic device for synthesis of nanomaterials. *Chem. Eng. J.* **2013**, *217*, 447–459.

(60) Fluent, A. 12.0 Theory Guide. *Ansys Inc* **2009**, *5* (5).

(61) Issa, R. I. Solution of the implicitly discretised fluid flow equations by operator-splitting. *J. Comput. Phys.* **1986**, *62* (1), 40–65.

(62) Leonard, B. P. A stable and accurate convective modelling procedure based on quadratic upstream interpolation. *Comput. Methods Appl. Mech. Eng.* **1979**, *19* (1), 59–98.

(63) Guo, Z.; Fletcher, D. F.; Haynes, B. S. Implementation of a height function method to alleviate spurious currents in CFD modelling of annular flow in microchannels. *Appl. Math. Model.* **2015**, *39* (16), 4665–4686.

(64) Stan, C. A.; Tang, S. K. Y.; Whitesides, G. M. Independent Control of Drop Size and Velocity in Microfluidic Flow-Focusing Generators Using Variable Temperature and Flow Rate. *Anal. Chem.* **2009**, *81* (6), 2399–2402.

(65) Cengel, Y. A.; Klein, S.; Beckman, W. *Heat transfer: a practical approach*; McGraw-Hill New York, 1998; Vol. 141.

(66) McAdams, W. H. *Heat Transmission: William H-McAdams*; McGraw-hill, 1954.

(67) Melissari, B.; Argyropoulos, S. A. Development of a heat transfer dimensionless correlation for spheres immersed in a wide range of Prandtl number fluids. *Int. J. Heat Mass Transf.* **2005**, *48* (21–22), 4333–4341.

(68) Bandara, T.; Nguyen, N.-T.; Rosengarten, G. Slug flow heat transfer without phase change in microchannels: A review. *Chem. Eng. Sci.* **2015**, *126*, 283–295.

(69) Mazutis, L.; Gilbert, J.; Ung, W. L.; Weitz, D. A.; Griffiths, A. D.; Heyman, J. A. Single-cell analysis and sorting using droplet-based microfluidics. *Nat. Protoc.* **2013**, *8* (5), 870.